

Entropy Stable Discontinuous Galerkin Methods for Balance Laws in Non-Conservative Form: Applications to the Euler Equations with Gravity

Maciej Waruszewski¹, Jeremy E. Kozdon¹, Lucas C. Wilcox¹, Thomas H. Gibson², Francis X. Giraldo¹

Abstract

In this work a non-conservative balance law formulation is considered that encompasses the rotating, compressible Euler equations for dry atmospheric flows. We develop a semi-discretely entropy stable discontinuous Galerkin method on curvilinear meshes using a generalization of flux differencing for numerical fluxes in fluctuation form. The method uses the skew-hybridized formulation of the element operators to ensure that, even in the presence of under-integration on curvilinear meshes, the resulting discretization is entropy stable. Several atmospheric flow test cases in one, two, and three dimensions confirm the theoretical entropy stability results as well as show the high-order accuracy and robustness of the method.

Keywords: Balance laws, Entropy stable, Discontinuous Galerkin, Geophysical flow

1. Introduction

Discontinuous Galerkin (DG) schemes for hyperbolic equations have many favorable properties, such as high-order accuracy, compact stencils, geometric flexibility, and the ability to add physical dissipation through upwind-biased numerical fluxes. DG belongs to the class of high-order element-based schemes [27, 30, 34] that can harness the fine-grained GPU parallelism needed for efficient exascale discretizations [1, 2, 33]. Due to their compact nature, DG schemes have demonstrated excellent scalability [42]. Provably stable DG discretizations can be constructed for linear systems [36, 62], and often work well for nonlinear systems with smooth and reasonably well-resolved solutions. However, in the presence of discontinuities and under-resolved phenomena, DG schemes often require additional stabilization. Classical stabilization techniques include dealiasing through over-integration [41], spectral filters [22], limiters [37, 43], and artificial viscosity [61, 65]. While these techniques enabled DG to perform complex simulations [5], they are not without drawbacks such as the possible loss of accuracy, hand-tuning of multiple parameters, and lack of a solid theoretical foundation.

Recently, entropy-stable DG schemes have emerged as a way to construct high-order discretizations with rigorous nonlinear stability estimates in a parameter-free fashion [25, 49]. Namely, semi-discrete entropy stability estimates are guaranteed by using specially constructed numerical fluxes [55] and flux-differencing [23]. Importantly, the schemes are computationally affordable because they do not rely on exact integration but instead exploit the summation-by-parts property of polynomial differentiation operators [24]. Following the pioneering work in Carpenter et al. [9], Gassner et al. [26] for the compressible Euler equations, the class of entropy-stable DG schemes has been extended to general systems of nonlinear conservation laws by Chen and Shu [16]. Chan [13, 14] generalized this to “modal” DG formulations which do not satisfy summation-by-parts. Most entropy stable DG schemes are constructed assuming exact integration in time, and Ranocha et al. [46] achieved fully discrete entropy-stability using relaxation Runge–Kutta time integrators.

The views expressed in this document are those of the authors and do not reflect the official policy or position of the Department of Defense or the U.S. Government.

Approved for public release; distribution unlimited

Email addresses: mwarusz@igf.fuw.edu.pl (Maciej Waruszewski), jekozdon@nps.edu (Jeremy E. Kozdon), lwilcox@nps.edu (Lucas C. Wilcox), thgibso2@illinois.edu (Thomas H. Gibson), fxgiraldo@nps.edu (Francis X. Giraldo)

¹Department of Applied Mathematics, Naval Postgraduate School, Monterey, CA, USA,

²National Center for Supercomputing Applications, Urbana, IL, USA,

Entropy-stable DG schemes have been constructed for many systems of nonlinear conservation and balance laws, such as the shallow water equations [63], the compressible multi-component Euler equations [48], special relativistic ideal magneto-hydrodynamics [21], and the ten-moment Gaussian closure equations [6]. However, many equations of physical interest do not conform to the standard balance law form and require extensions of the basic entropy-stability framework. Entropy-stable treatment of non-conservative source terms appearing in certain formulations of magneto-hydrodynamics has been presented in Liu et al. [38] for the ideal equations and in Bohm et al. [8] for the resistive equations. Renac [47] constructed an entropy-stable DG spectral element scheme for a one-dimensional, nonlinear hyperbolic system in non-conservative form and applied it to two-phase flow. Coquel et al. [18] then used this framework for the Baer–Nunziato two-phase flow model.

The motivation for this paper is the construction of entropy stable schemes for the Euler equations with gravity. These equations are of fundamental importance in simulations of astrophysical phenomena, atmospheric large-eddy simulations, numerical weather prediction, and climate modeling. Due to their excellent properties, DG schemes are already emerging in computational astrophysics [32, 50] as well as in small- and large-scale atmospheric modeling [3, 29, 40, 58]. In contrast to engineering applications, many atmospheric models formulate the equations in terms of an entropy-type variable known as potential temperature, which has favorable properties for simulating atmospheric flows [53]. However, in climate modeling applications, conservation of total energy and balanced energy transfers are also of great interest. This can be achieved, for example, by using mimetic methods [56]. An alternative, that we propose in this paper, is to guarantee conservation of energy by using the total energy formulation, and use the entropy-stable approach for robustness and consistency with the second law of thermodynamics. Crucially, this requires an extension of the existing entropy-stable framework, since in the total energy formulation of the Euler equations the gravity force enters as a non-conservative and spatially varying source term.

To do this we recast the Euler equations with gravity in a more general, non-conservative balance law formulation. We then construct arbitrary order flux differencing DG schemes for this balance law formulation and give conditions that the numerical fluxes must satisfy to ensure entropy stability. We present, in explicit form, an entropy-conserving numerical flux for the Euler equations with gravity and show how to modify it to make it entropy-stable. A variation on the classical one-dimensional Sod shock tube benchmark, put into a gravitational field, is used to show the versatility of the scheme in terms of choice of basis and quadrature rule. Two-dimensional atmospheric test cases of buoyant convection and gravity wave propagation verify, respectively, the entropy-conservation and high-order accuracy of the scheme. Finally, a baroclinic wave benchmark on the sphere demonstrates the robustness of the scheme for long-time simulations of idealized weather-like phenomena in a curvilinear three-dimensional geometry.

2. Balance law formulation

The rotating, compressible Euler equations for dry atmospheric flows in d dimensions ($d = 1, 2, 3$) are

$$\frac{\partial \rho}{\partial t} + \sum_{k=1}^d \frac{\partial \rho u_k}{\partial x_k} = 0, \quad (1a)$$

$$\frac{\partial \rho u_i}{\partial t} + \sum_{k=1}^d \frac{\partial \rho u_i u_k}{\partial x_k} + \frac{\partial p}{\partial x_i} + \rho \frac{\partial \phi}{\partial x_i} = -2 \sum_{j,k=1}^d \varepsilon_{ijk} \omega_j u_k, \quad i = 1, \dots, d, \quad (1b)$$

$$\frac{\partial \rho e}{\partial t} + \sum_{k=1}^d \frac{\partial u_k (\rho e + p)}{\partial x_k} = 0. \quad (1c)$$

Here the prognostic variables are density ρ , momentum ρu_i for $i = 1, \dots, d$, and total energy ρe . The pressure p is

$$p = (\gamma - 1) \left(\rho e - \rho \phi - \frac{1}{2} \sum_{j=1}^d \rho u_j^2 \right), \quad (2)$$

where ϕ is a spatially varying geopotential function and the constant $\gamma = \frac{c_p}{c_v}$ is the specific heat ratio given in terms of the specific heats for constant pressure and volume, c_p and c_v , respectively; we take $\gamma = 7/5$. The components of a

(potentially spatially varying) planetary rotation vector are ω_i for $i = 1, \dots, d$. The Coriolis source term is given as twice the cross product of the rotation vector with the fluid velocity, expressed using the Levi–Civita symbol

$$\varepsilon_{ijk} = \begin{cases} +1, & \text{if } ijk \text{ is } 123, 312, \text{ or } 231, \\ -1, & \text{if } ijk \text{ is } 321, 132, \text{ or } 213, \\ 0, & \text{otherwise.} \end{cases} \quad (3)$$

For the problem defined by equations (1) to be well-posed, hyperbolic, and physically meaningful, density and pressure must be positive.

Designing an entropy stable discretization of governing equations (1) is challenging because of the presence of the geopotential in the gravitational source and the pressure gradient term. It is possible to rewrite (1) as a pure conservation law [17], but it necessitates introduction of global fluxes, which are problematic for Godunov methods. Here, we consider a generalized balance law formulation of the form

$$\frac{\partial \mathbf{q}(\mathbf{x}, t)}{\partial t} + \sum_{i=1}^d \mathbf{A}_i(\mathbf{q}(\mathbf{x}, t), \mathbf{x}) \frac{\partial \mathbf{h}_i(\mathbf{q}(\mathbf{x}, t), \mathbf{x})}{\partial x_i} = \mathbf{g}(\mathbf{q}(\mathbf{x}, t), \mathbf{x}), \quad (4)$$

which will facilitate designing an entropy stable method. Here, $\mathbf{q}(\mathbf{x}, t)$ is the solution vector of length N_c , the total number of prognostic variables. Additionally, $\mathbf{h}_i(\mathbf{q}, \mathbf{x}) \in \mathbb{R}^{N_d}$ is a vector-valued function and $\mathbf{A}_i(\mathbf{q}, \mathbf{x}) \in \mathbb{R}^{N_c \times N_d}$ is a matrix-valued function, where in order to allow modeling flexibility N_d is allowed to be different from N_c ; for conservation laws $N_d = N_c$ and $\mathbf{A}_i = I$ with \mathbf{h}_i being the flux function. Balance law formulation (4) allows for source terms to be included in $\mathbf{A}_i \frac{\partial \mathbf{h}_i}{\partial x_i}$ or the vector-valued function $\mathbf{g}(\mathbf{q}, \mathbf{x}) \in \mathbb{R}^{N_c}$.

With $d = 3$ the atmospheric equations (1) can be written in balance law form (4) by defining the solution vector

$$\mathbf{q} = [\rho \quad \rho u_1 \quad \rho u_2 \quad \rho u_3 \quad \rho e]^T. \quad (5)$$

The matrix function \mathbf{A}_k and vector function \mathbf{h}_k for $k = 1, 2, 3$ have $N_d = 6$ and are defined as

$$\mathbf{A}_k(\mathbf{q}, \mathbf{x}) = \begin{bmatrix} 1 & 0 & 0 & 0 & 0 & 0 \\ 0 & 1 & 0 & 0 & 0 & \delta_{1k}\rho \\ 0 & 0 & 1 & 0 & 0 & \delta_{2k}\rho \\ 0 & 0 & 0 & 1 & 0 & \delta_{3k}\rho \\ 0 & 0 & 0 & 0 & 1 & 0 \end{bmatrix}, \quad \mathbf{h}_k(\mathbf{q}, \mathbf{x}) = \begin{bmatrix} \rho u_k \\ \rho u_1 u_k + \delta_{1k} p \\ \rho u_2 u_k + \delta_{2k} p \\ \rho u_3 u_k + \delta_{3k} p \\ u_k(\rho e + p) \\ \phi \end{bmatrix}, \quad (6)$$

with δ_{ik} being the Kronecker delta. The source term is

$$\mathbf{g}(\mathbf{q}, \mathbf{x}) = \sum_{j,k=1}^d \begin{bmatrix} 0 \\ -2\varepsilon_{1jk}\omega_j u_k \\ -2\varepsilon_{2jk}\omega_j u_k \\ -2\varepsilon_{3jk}\omega_j u_k \\ 0 \end{bmatrix}; \quad (7)$$

note that only the Coriolis term is included in the source and the geopotential is included in the differential term.

3. Entropy analysis

Here we summarize continuous entropy results needed for the discrete analysis that follows; for a more complete overview of the theory see, for example, Dafermos [19, Sections 1.4, 1.5, 3.1, and 3.2].

3.1. Companion balance law

We assume that balance law (4) is endowed with a nontrivial companion balance law

$$\frac{\partial \eta(\mathbf{q}(\mathbf{x}, t), \mathbf{x})}{\partial t} + \sum_{j=1}^d \frac{\partial \zeta_j(\mathbf{q}(\mathbf{x}, t), \mathbf{x})}{\partial x_j} = \Pi(\mathbf{q}(\mathbf{x}, t), \mathbf{x}), \quad (8)$$

where η is a scalar convex entropy function and ζ_j are associated entropy fluxes. This assumption is valid for many systems of balance laws from continuum physics which typically have a natural companion balance law related to the second law of thermodynamics, e.g., Dafermos [19, Section 3.3]. Specifically, companion balance law (8) provides an entropy balance constraint on the solution of balance law (4). The vector of entropy variables $\boldsymbol{\beta}$ is obtained by differentiating the entropy function with respect to the state \mathbf{q} . That is, $\boldsymbol{\beta} = \frac{\partial \eta}{\partial \mathbf{q}}$, with component $\alpha = 1, \dots, N_c$ given by

$$\beta_\alpha(\mathbf{q}, \mathbf{x}) = \frac{\partial \eta(\mathbf{q}, \mathbf{x})}{\partial q_\alpha}. \quad (9)$$

To obtain an entropy balance condition, we first contract the balance law (4) with the entropy variables (9),

$$\frac{\partial \eta(\mathbf{q}, \mathbf{x})}{\partial t} + \sum_{i=1}^d \boldsymbol{\beta}^T(\mathbf{q}, \mathbf{x}) A_i(\mathbf{q}, \mathbf{x}) \frac{\partial \mathbf{h}_i(\mathbf{q}, \mathbf{x})}{\partial x_i} = \boldsymbol{\beta}^T(\mathbf{q}, \mathbf{x}) \mathbf{g}(\mathbf{q}, \mathbf{x}). \quad (10)$$

Comparing (10) with the companion balance law (8) gives

$$\frac{\partial \zeta_j(\mathbf{q}, \mathbf{x})}{\partial q_\alpha} = \boldsymbol{\beta}^T(\mathbf{q}, \mathbf{x}) A_j(\mathbf{q}, \mathbf{x}) \frac{\partial \mathbf{h}_j(\mathbf{q}, \mathbf{x})}{\partial q_\alpha}, \quad (11)$$

when the entropy production function is taken as

$$\Pi(\mathbf{q}, \mathbf{x}) = \boldsymbol{\beta}(\mathbf{q}, \mathbf{x})^T \mathbf{g}(\mathbf{q}, \mathbf{x}) + \sum_{i=1}^d \left(\frac{\partial \zeta_i(\mathbf{q}, \mathbf{x})}{\partial x_i} - \boldsymbol{\beta}^T(\mathbf{q}, \mathbf{x}) A_i(\mathbf{q}, \mathbf{x}) \frac{\partial \mathbf{h}_i(\mathbf{q}, \mathbf{x})}{\partial x_i} \right). \quad (12)$$

We will restrict ourselves to equations for which the summation term is exactly zero so that $\Pi(\mathbf{q}, \mathbf{x}) = \boldsymbol{\beta}(\mathbf{q}, \mathbf{x})^T \mathbf{g}(\mathbf{q}, \mathbf{x})$.

Classical (Lipschitz continuous) solutions that satisfy the balance law (4) (almost everywhere) are automatically (classical) solutions of the companion balance law (8). Integrating (8) over the domain Ω with boundary $\partial\Omega$ and outward unit normal \mathbf{n} gives the continuous entropy balance equality

$$\int_{\Omega} \frac{\partial \eta(\mathbf{q}, \mathbf{x})}{\partial t} d\mathbf{x} + \sum_{j=1}^d \int_{\partial\Omega} n_j \zeta_j(\mathbf{q}, \mathbf{x}) dS = \int_{\Omega} \Pi(\mathbf{q}, \mathbf{x}) d\mathbf{x}. \quad (13)$$

Dafermos [19, Section 1.5] further states that one of the tenets of the theory of balance laws is that admissible weak solutions should at least satisfy

$$\frac{\partial \eta(\mathbf{q}(\mathbf{x}, t), \mathbf{x})}{\partial t} + \sum_{j=1}^d \frac{\partial \zeta_j(\mathbf{q}(\mathbf{x}, t), \mathbf{x})}{\partial x_j} \leq \Pi(\mathbf{q}(\mathbf{x}, t), \mathbf{x}) \quad (14)$$

in the sense of distributions. Integrating this over the domain gives:

$$\int_{\Omega} \frac{\partial \eta(\mathbf{q}, \mathbf{x})}{\partial t} d\mathbf{x} + \sum_{j=1}^d \int_{\partial\Omega} n_j \zeta_j(\mathbf{q}, \mathbf{x}) dS \leq \int_{\Omega} \Pi(\mathbf{q}, \mathbf{x}) d\mathbf{x}. \quad (15)$$

The primary objective of semi-discrete entropy analysis is to ensure a discrete analogue of entropy balance (13) and dissipation (15).

3.2. Entropy for the atmospheric Euler equations

For the atmospheric Euler equations (1), we define the convex mathematical entropy function

$$\eta = -\frac{\rho s}{\gamma - 1}, \quad (16)$$

where $s = \log(p/\rho^\gamma)$ is the specific (physical) entropy. The components of the entropy flux (11) are taken to be

$$\zeta_j = u_j \eta. \quad (17)$$

The entropy variables (9) are obtained with η defined by (16) resulting in

$$\beta_1 = \frac{\gamma - s}{\gamma - 1} - (u_1^2 + u_2^2 + u_3^2 - 2\phi)b, \quad (18a)$$

$$\beta_2 = 2bu_1, \quad (18b)$$

$$\beta_3 = 2bu_2, \quad (18c)$$

$$\beta_4 = 2bu_3, \quad (18d)$$

$$\beta_5 = -2b, \quad (18e)$$

with $b = \rho/2p$ is the inverse temperature. Recognizing that $b = -\beta_5/2$, the prognostic state can be recovered from the entropy variables using

$$u_1 = \frac{\beta_2}{2b}, \quad (19a)$$

$$u_2 = \frac{\beta_3}{2b}, \quad (19b)$$

$$u_3 = \frac{\beta_4}{2b}, \quad (19c)$$

$$e = \frac{1}{(\gamma - 1)2b} + \frac{u_1^2 + u_2^2 + u_3^2}{2} + \phi, \quad (19d)$$

$$\rho = \left(2b \exp\left((\gamma - 1) \left(-\beta_1 + \left(2\phi - (u_1^2 + u_2^2 + u_3^2) \right) b \right) + \gamma \right) \right)^{-1/(\gamma - 1)}. \quad (19e)$$

When pressure and density are both positive the mapping between entropy and conserved variables is well-defined. Using explicit forms of the source term (7) and the entropy variables (18) the entropy production for the atmospheric Euler equations (1) is $\Pi = \boldsymbol{\beta}^T \mathbf{g} = -2b\epsilon_{ijk}\omega_j u_i u_k = 0$, which is zero due to skew symmetry of ϵ (3). This result also simply follows from the fact that the Coriolis force is an inertial force.

4. Flux differencing discontinuous Galerkin methods

In this section we establish our notation and a flux differencing formulation for balance law (4); our notation is motivated by Castro et al. [11], Chan [13, 14], Renac [47].

4.1. Notation

Let the domain Ω be tessellated by a mesh of disjoint elements $K \subset \mathbb{R}^d$ with boundaries ∂K , where each polygonal element K is mapped to a reference element \hat{K} with boundary $\partial \hat{K}$. Points on the physical and reference elements are denoted as \mathbf{x} and $\boldsymbol{\xi}$, respectively. The outward unit normal in the physical coordinate system is \mathbf{n} with $\hat{\mathbf{n}}$ denoting the unit normal to $\partial \hat{K}$.

For each element K , we assume there is a suitably smooth (differentiable) transformation between the physical and reference element. For a given function $u(\mathbf{x})$ defined on a physical element K , we denote its mapping to the reference element \hat{K} as $\hat{u}(\boldsymbol{\xi})$. We let $J^v(\boldsymbol{\xi})$ be the Jacobian determinant of the volume transformation, $J^f(\boldsymbol{\xi})$ the Jacobian

determinant of the surface mapping, and $\hat{J}^f(\boldsymbol{\xi})$ the Jacobian determinant of the associated reference face. Using these Jacobian factors, integrals over physical elements in terms of integrals on the reference element are

$$\int_K u(\mathbf{x}) \, d\mathbf{x} = \int_{\hat{K}} J^v(\boldsymbol{\xi}) \hat{u}(\boldsymbol{\xi}) \, d\hat{\mathbf{x}}, \quad (20)$$

$$\int_{\partial K} u(\mathbf{x}) \, dS = \int_{\partial \hat{K}} J^f(\boldsymbol{\xi}) \hat{u}(\boldsymbol{\xi}) \, d\hat{S}. \quad (21)$$

The reference and physical outward unit normals are related by

$$J^f \mathbf{n}_i = \sum_{k=1}^d J^v \frac{\partial \xi_i}{\partial x_k} \hat{\mathbf{n}}_k \hat{J}_k^f. \quad (22)$$

On the reference element we assume that functions are approximated in some polynomial space $\mathbb{K}^N = \mathbb{K}^N(\hat{K})$, where N is the degree of approximation. In the numerical results we use tensor product (interval, quadrilateral, and hexahedral) elements to represent the computational domain, and \mathbb{K}^N is selected to be the space of d -dimensional tensor product polynomials of degree N in each dimension. However, the analysis that follows is more general and can be applied to other elements types, e.g., simplices; see Chan [14] for a fuller discussion of other element types. Specifically, in the definition of the operators there is no assumption that the interpolation and quadrature points are collocated. Additionally, we do not assume that the surface quadrature points are a subset of the volume quadrature points. That said, when Legendre–Gauss–Lobatto points are used for interpolation and quadrature, e.g., a spectral element method, many of the operators simplify; see Remark 1 below.

We let $\{v_i(\boldsymbol{\xi})\}_{i=1}^{N_p}$ denote a basis for \mathbb{K}^N , where N_p is the dimensionality of the space. Any function $q^N(\boldsymbol{\xi}) \in \mathbb{K}^N$ can therefore be represented as

$$q^N(\boldsymbol{\xi}) = \boldsymbol{\Upsilon}^T(\boldsymbol{\xi}) \mathbf{q}^N, \quad (23)$$

where $\boldsymbol{\Upsilon}(\boldsymbol{\xi})$ is a vector of basis functions and \mathbf{q}^N is a vector of expansion coefficients.

4.2. Skew-hybridized summation-by-parts operators

Following Chan [14], we construct skew-hybridized operators involving both volume and surface quadrature nodes. Here we highlight the notation needed in this paper; further details and discussion on the operators' accuracy requirements can be found in Chan [14]. Throughout we use the notation $[\cdot]_n$ and $[\cdot]_{n,m}$ to denote the elements of a vector and matrix, respectively.

The volume and surface quadrature rules on the reference element \hat{K} are $([\boldsymbol{\xi}^v]_i, [\mathbf{w}^v]_i)_{i=1}^{N_q^v}$ and $([\boldsymbol{\xi}^f]_i, [\mathbf{w}^f]_i)_{i=1}^{N_q^f}$, with N_q^v and N_q^f being the total number of volume and surface quadrature points, respectively. Here $\boldsymbol{\xi}^v$ and $\boldsymbol{\xi}^f$ denote vectors of quadrature points, while \mathbf{w}^v and \mathbf{w}^f are the weights. Diagonal matrices of the quadrature weights are

$$\mathbf{W}^v = \text{diag}(\mathbf{w}^v), \quad \mathbf{W}^f = \text{diag}(\mathbf{w}^f). \quad (24)$$

Similarly, we define diagonal matrices of the volume and surface Jacobians evaluated at the quadrature points,

$$\mathbf{J}^v = \text{diag}(J^v(\boldsymbol{\xi}^v)), \quad \mathbf{J}^f = \text{diag}(J^f(\boldsymbol{\xi}^f)). \quad (25)$$

As discussed later, J^v and J^f are often not exact but approximations in \mathbb{K}^N .

Vandermonde matrices for the volume $\mathbf{V}^v \in \mathbb{R}^{N_q^v \times N_p}$ and surface $\mathbf{V}^f \in \mathbb{R}^{N_q^f \times N_p}$ that interpolate the expansion coefficients to the quadrature points have elements

$$[\mathbf{V}^v]_{n,m} = v_m([\boldsymbol{\xi}^v]_n), \quad [\mathbf{V}^f]_{n,m} = v_m([\boldsymbol{\xi}^f]_n). \quad (26)$$

The combined quadrature Vandermonde matrix

$$\mathbf{V} = \begin{bmatrix} \mathbf{V}^v \\ \mathbf{V}^f \end{bmatrix}, \quad (27)$$

interpolates from the expansion coefficients to the volume and surface quadrature points. With the above notation the volume mass matrix

$$\mathbf{M}^v = (\mathbf{V}^v)^T \mathbf{W}^v \mathbf{J}^v \mathbf{V}^v, \quad (28)$$

is defined to approximate inner products of functions in \mathbb{K}^N on the reference element in physical space.

In order to project functions defined on the volume quadrature points to polynomials in \mathbb{K}^N we define a *quadrature-based L^2 projection operator*

$$\mathbf{P}^v = (\mathbf{M}^v)^{-1} (\mathbf{V}^v)^T \mathbf{J}^v \mathbf{W}^v. \quad (29)$$

We observe that going from the expansion coefficients to the quadrature points and back is exact:

$$\mathbf{P}^v \mathbf{V}^v = \mathbf{I}. \quad (30)$$

The polynomial differentiation matrix with respect to the i -th reference coordinate is $\mathbf{D}_i^N \in \mathbb{R}^{N_p \times N_p}$. Namely, if \mathbf{q} are the expansion coefficients of $q^N \in \mathbb{K}^N$, then $\mathbf{D}_i^N \mathbf{q}^N$ are the expansion coefficients for $\frac{\partial q^N}{\partial \xi_i} \in \mathbb{K}^N$. The *quadrature-based volume integrated differentiation operator* with respect to the i -th reference coordinate is

$$\mathbf{Q}_i^v = \mathbf{W}^v \mathbf{V}^v \mathbf{D}_i^N \mathbf{P}^v. \quad (31)$$

With this, we follow Chan [14] and define the skew-hybridized summation-by-parts (SBP) operator

$$\mathbf{Q}_i = \frac{1}{2} \begin{bmatrix} \mathbf{Q}_i^v - (\mathbf{Q}_i^v)^T & (\mathbf{E}^v)^T \mathbf{B}_i^f \\ -\mathbf{B}_i^f \mathbf{E}^v & \mathbf{B}_i^f \end{bmatrix}. \quad (32)$$

Here the matrix $\mathbf{E}^v = \mathbf{V}^f \mathbf{P}^v$ projects between the volume quadrature to the face quadrature and $\mathbf{B}_i^f = \mathbf{W}^f \hat{\mathbf{N}}_i^f \hat{\mathbf{J}}^f$ is the reference normal-weighted surface quadrature with $\hat{\mathbf{N}}_i^f$ being the diagonal matrix of component i of $\hat{\mathbf{n}}$ and $\hat{\mathbf{J}}^f$ being the reference face Jacobian determinant, all evaluated at the surface quadrature points. Since $\mathbf{Q}_i \in \mathbb{R}^{(N_q^v + N_q^f) \times (N_q^v + N_q^f)}$ it operates on functions defined on the combined volume and surface quadratures.

The skew-hybridized SBP operator is almost skew-symmetric, as characterized by the following lemma from Chan [14, Lemma 1].

Lemma 1 (The skew-hybridized SBP operator). *The skew-hybridized SBP operator \mathbf{Q}_i satisfies the generalized summation-by-parts (SBP) property:*

$$\mathbf{Q}_i + \mathbf{Q}_i^T = \begin{bmatrix} \mathbf{0} & \\ & \mathbf{B}_i^f \end{bmatrix}. \quad (33)$$

The reason for \mathbf{Q}_i being referred to as an SBP operator is because the discrete identity

$$\left(\mathbf{p}^N \right)^T \mathbf{V}^T \left(\mathbf{Q}_i + \mathbf{Q}_i^T \right) \mathbf{V} \mathbf{q}^N = \left(\mathbf{V}^f \mathbf{p}^N \right)^T \mathbf{W}^f \hat{\mathbf{N}}_i^f \mathbf{J}_i^f \mathbf{V}^f \mathbf{q}^N, \quad (34)$$

is an approximation of the continuous multidimensional integration-by-parts identity

$$\int_{\hat{\mathcal{K}}} \left(\frac{\partial p}{\partial \xi_i} q + p \frac{\partial q}{\partial \xi_i} \right) d\hat{\mathbf{x}} = \int_{\partial \hat{\mathcal{K}}} \hat{n}_i p q d\hat{\mathcal{S}}. \quad (35)$$

The advantage of using \mathbf{Q}_i is that one is *guaranteed* to satisfy the SBP property, no matter the degree of accuracy of the volume and surface quadrature rules. This allows for the construction of SBP operators in spite of aliasing errors due to inexact integration [14, 24, 45]. Later we will assume consistency for the skew-hybridized SBP operator; see Chan [14] for required accuracy conditions.

Assumption 1. The skew-hybridized SBP operator is assumed to be exact for constants:

$$\mathbf{Q}_i \mathbf{1} = \mathbf{0}. \quad (36)$$

Diagonal matrices of the metric terms evaluated at volume and surface quadrature points are

$$\mathbf{G}_{jk}^v = \text{diag}\left(J^v \frac{\partial \xi_j}{\partial x_k}(\xi^v)\right), \quad \mathbf{G}_{jk}^f = \text{diag}\left(J^v \frac{\partial \xi_j}{\partial x_k}(\xi^f)\right), \quad (37)$$

respectively. Their combined matrix is

$$\mathbf{G}_{jk} = \begin{bmatrix} \mathbf{G}_{jk}^v & \\ & \mathbf{G}_{jk}^f \end{bmatrix}. \quad (38)$$

As noted above, these are often approximated using the discrete operators. One benefit of this is that the volume \mathbf{G}_{jk}^v and surface \mathbf{G}_{jk}^f can be defined in a consistent manner, e.g., $\mathbf{G}_{jk}^f = \text{diag}\left(\mathbf{E}^v \bar{\mathbf{G}}_{jk}^v\right)$ where $\bar{\mathbf{G}}_{jk}^v$ is the diagonal of \mathbf{G}_{jk}^v interpreted as a vector.

In the discrete entropy stability analysis we will require that the metrics discretely satisfy the geometric conservation law [35, 57]

$$\sum_{k=1}^d \mathbf{Q}_k \mathbf{G}_{jk} \mathbf{1} = \mathbf{0}, \quad (39)$$

which is a discrete statement of the continuous metric identity

$$\sum_{k=1}^d \frac{\partial}{\partial \xi_k} \left(J \frac{\partial \xi_k}{\partial x_j} \right) = 0. \quad (40)$$

4.3. Flux differencing in fluctuation form

Motivated by Castro et al. [11] and Renac [47] we define a numerical flux function in fluctuation form as

$$\begin{aligned} \mathcal{D}_i(\mathbf{p}, \mathbf{y}, \mathbf{q}, \mathbf{x}) &= \mathcal{A}_i(\mathbf{p}, \mathbf{y}, \mathbf{q}, \mathbf{x}) \mathcal{H}_i(\mathbf{p}, \mathbf{y}, \mathbf{q}, \mathbf{x}) + \mathcal{A}_i(\mathbf{q}, \mathbf{x}, \mathbf{p}, \mathbf{y}) \mathcal{H}_i(\mathbf{q}, \mathbf{x}, \mathbf{p}, \mathbf{y}) \\ &\quad - (\mathcal{A}_i(\mathbf{p}, \mathbf{y}, \mathbf{q}, \mathbf{x}) + \mathcal{A}_i(\mathbf{q}, \mathbf{x}, \mathbf{p}, \mathbf{y})) \mathbf{h}_i(\mathbf{p}, \mathbf{y}). \end{aligned} \quad (41)$$

The matrix-valued function $\mathcal{A}_i(\mathbf{p}, \mathbf{y}, \mathbf{q}, \mathbf{x})$ and vector-valued function $\mathcal{H}_i(\mathbf{p}, \mathbf{y}, \mathbf{q}, \mathbf{x})$ are assumed to satisfy the consistency conditions

$$2\mathcal{A}_i(\mathbf{q}, \mathbf{x}, \mathbf{q}, \mathbf{x}) = \mathbf{A}_i(\mathbf{q}, \mathbf{x}), \quad (42)$$

$$\mathcal{H}_i(\mathbf{q}, \mathbf{x}, \mathbf{q}, \mathbf{x}) = \mathbf{h}_i(\mathbf{q}, \mathbf{x}). \quad (43)$$

In the special case of balance law (4) being a conservation law, i.e., $\mathbf{A}_i = \mathbf{I}$ and $\mathbf{h}_i = \mathbf{f}_i$, we can choose $\mathcal{A}_i(\mathbf{p}, \mathbf{y}, \mathbf{q}, \mathbf{x}) = \mathbf{I}/2$ and let $\mathcal{F}_i(\mathbf{p}, \mathbf{y}, \mathbf{q}, \mathbf{x})$ be a symmetric and consistent numerical flux so that

$$\mathcal{D}_i^{\text{cons}}(\mathbf{p}, \mathbf{y}, \mathbf{q}, \mathbf{x}) = \mathcal{F}_i(\mathbf{p}, \mathbf{y}, \mathbf{q}, \mathbf{x}) - \mathbf{f}_i(\mathbf{p}, \mathbf{y}). \quad (44)$$

The following lemma relates the derivative of the numerical flux function \mathcal{D}_i to the spatial derivatives in balance law (4), i.e., a flux differencing form of the derivative.

Lemma 2. *If numerical flux \mathcal{D}_i defined by (41) satisfies consistency conditions (42) and (43) then*

$$2 \frac{\partial \mathcal{D}_i(\mathbf{q}(\mathbf{y}), \mathbf{y}, \mathbf{q}(\mathbf{x}), \mathbf{x})}{\partial x_j} \Big|_{\mathbf{y}=\mathbf{x}} = \mathbf{A}_i(\mathbf{q}(\mathbf{x}), \mathbf{x}) \frac{\partial \mathbf{h}_i(\mathbf{q}(\mathbf{x}), \mathbf{x})}{\partial x_j} \quad (45)$$

and

$$\begin{aligned} &\mathbf{p}(\mathbf{x})^T \mathbf{A}_j(\mathbf{q}(\mathbf{x}), \mathbf{x}) \frac{\partial \mathbf{h}(\mathbf{q}(\mathbf{x}), \mathbf{x})}{\partial x_j} \\ &= \frac{\partial}{\partial x_j} \left(\mathbf{p}(\mathbf{y})^T \mathcal{D}_i(\mathbf{q}(\mathbf{y}), \mathbf{y}, \mathbf{q}(\mathbf{x}), \mathbf{x}) - \mathbf{p}(\mathbf{x})^T \mathcal{D}_i(\mathbf{q}(\mathbf{x}), \mathbf{x}, \mathbf{q}(\mathbf{y}), \mathbf{y}) \right) \Big|_{\mathbf{y}=\mathbf{x}}. \end{aligned} \quad (46)$$

PROOF. Identity (45) follows from the consistency conditions:

$$\begin{aligned}
& A_i(\mathbf{q}(x), \mathbf{x}) \frac{\partial \mathbf{h}_i(\mathbf{q}(x), \mathbf{x})}{\partial x_j} \\
&= \frac{\partial A_i(\mathbf{q}(x), \mathbf{x}) \mathbf{h}_i(\mathbf{q}(x), \mathbf{x})}{\partial x_j} - \frac{\partial A_i(\mathbf{q}(x), \mathbf{x})}{\partial x_j} \mathbf{h}_i(\mathbf{q}(x), \mathbf{x}) \\
&= \frac{\partial}{\partial x_j} (A_i(\mathbf{q}(x), \mathbf{x}) (\mathbf{h}_i(\mathbf{q}(x), \mathbf{x}) - \mathbf{h}_i(\mathbf{q}(y), \mathbf{y}))) \Big|_{\mathbf{y}=\mathbf{x}} \\
&= 2 \frac{\partial}{\partial x_j} (\mathcal{A}_i(\mathbf{q}(x), \mathbf{x}, \mathbf{q}(x), \mathbf{x}) (\mathcal{H}_i(\mathbf{q}(x), \mathbf{x}, \mathbf{q}(x), \mathbf{x}) - \mathbf{h}_i(\mathbf{q}(y), \mathbf{y}))) \Big|_{\mathbf{y}=\mathbf{x}} \\
&= 2 \frac{\partial}{\partial x_j} (\mathcal{A}_i(\mathbf{q}(y), \mathbf{y}, \mathbf{q}(x), \mathbf{x}) (\mathcal{H}_i(\mathbf{q}(y), \mathbf{y}, \mathbf{q}(x), \mathbf{x}) - \mathbf{h}_i(\mathbf{q}(y), \mathbf{y}))) \Big|_{\mathbf{y}=\mathbf{x}} \\
&\quad + 2 \frac{\partial}{\partial x_j} (\mathcal{A}_i(\mathbf{q}(x), \mathbf{x}, \mathbf{q}(y), \mathbf{y}) (\mathcal{H}_i(\mathbf{q}(x), \mathbf{x}, \mathbf{q}(y), \mathbf{y}) - \mathbf{h}_i(\mathbf{q}(y), \mathbf{y}))) \Big|_{\mathbf{y}=\mathbf{x}} \\
&= 2 \frac{\partial}{\partial x_j} \mathcal{D}_i(\mathbf{q}(y), \mathbf{y}, \mathbf{q}(x), \mathbf{x}) \Big|_{\mathbf{y}=\mathbf{x}}.
\end{aligned} \tag{47}$$

Consistency implies that $\mathcal{D}_i(\mathbf{q}, \mathbf{x}, \mathbf{q}, \mathbf{x}) = \mathbf{0}$, which when combined with (45) implies (46):

$$\begin{aligned}
& \mathbf{p}(x)^T A_j(\mathbf{q}(x), \mathbf{x}) \frac{\partial \mathbf{h}(\mathbf{q}(x), \mathbf{x})}{\partial x_j} \\
&= 2 \mathbf{p}(x)^T \frac{\partial \mathcal{D}_i(\mathbf{q}(y), \mathbf{y}, \mathbf{q}(x), \mathbf{x})}{\partial x_j} \Big|_{\mathbf{y}=\mathbf{x}} \\
&= \left(2 \mathbf{p}(y)^T \frac{\partial \mathcal{D}_i(\mathbf{q}(y), \mathbf{y}, \mathbf{q}(x), \mathbf{x})}{\partial x_j} \right) \Big|_{\mathbf{y}=\mathbf{x}} - \frac{\partial \mathbf{p}(x)^T \mathcal{D}_i(\mathbf{q}(x), \mathbf{x}, \mathbf{q}(x), \mathbf{x})}{\partial x_j} \\
&= \left(\mathbf{p}(y)^T \frac{\partial \mathcal{D}_i(\mathbf{q}(y), \mathbf{y}, \mathbf{q}(x), \mathbf{x})}{\partial x_j} - \frac{\partial \mathbf{p}(x)^T \mathcal{D}_i(\mathbf{q}(x), \mathbf{x}, \mathbf{q}(y), \mathbf{y})}{\partial x_j} \right) \Big|_{\mathbf{y}=\mathbf{x}} \\
&= \frac{\partial}{\partial x_j} \left(\mathbf{p}(y)^T \mathcal{D}_i(\mathbf{q}(y), \mathbf{y}, \mathbf{q}(x), \mathbf{x}) - \mathbf{p}(x)^T \mathcal{D}_i(\mathbf{q}(x), \mathbf{x}, \mathbf{q}(y), \mathbf{y}) \right) \Big|_{\mathbf{y}=\mathbf{x}}.
\end{aligned} \tag{48}$$

□

For conservation laws we have the following theorem showing the equivalence to the conservation law flux differencing [13].

Theorem 3. *If the numerical flux (44) is used then*

$$\frac{\partial \mathcal{D}_i^{\text{cons}}(\mathbf{q}(y), \mathbf{y}, \mathbf{q}(x), \mathbf{x})}{\partial x_j} \Big|_{\mathbf{y}=\mathbf{x}} = \frac{\partial \mathcal{F}_i(\mathbf{q}(y), \mathbf{y}, \mathbf{q}(x), \mathbf{x})}{\partial x_j} \Big|_{\mathbf{y}=\mathbf{x}}. \tag{49}$$

In Renac [47] the case of $\mathbf{h}_i(\mathbf{q}, \mathbf{x}) = \mathbf{q}$ was considered, and the above formulation is equivalent when $\mathcal{H}_i^{\text{Renac}}(\mathbf{p}, \mathbf{y}, \mathbf{q}, \mathbf{x}) = \mathbf{q}$ in which case the numerical flux reduces to

$$\mathcal{D}_i^{\text{Renac}}(\mathbf{p}, \mathbf{y}, \mathbf{q}, \mathbf{x}) = \mathcal{A}_i^{\text{Renac}}(\mathbf{p}, \mathbf{y}, \mathbf{q}, \mathbf{x})(\mathbf{q} - \mathbf{p}). \tag{50}$$

4.4. Discontinuous Galerkin methods with flux differencing in fluctuation form

To derive a flux differencing scheme we begin with a “strong derivative” DG scheme for balance law (4) for a single element K ,

$$\begin{aligned} & \int_K \mathbf{p}(\mathbf{x})^T \frac{\partial \mathbf{q}(\mathbf{x}, t)}{\partial t} d\mathbf{x} + \sum_{j=1}^d \int_K \mathbf{p}(\mathbf{x})^T A_j(\mathbf{q}(\mathbf{x}, t), \mathbf{x}) \frac{\partial \mathbf{h}(\mathbf{q}(\mathbf{x}, t), \mathbf{x})}{\partial x_j} d\mathbf{x} \\ &= \int_K \mathbf{p}(\mathbf{x})^T \mathbf{g}(\mathbf{q}(\mathbf{x}, t), \mathbf{x}) d\mathbf{x} - \sum_{j=1}^d \int_{\partial K} \mathbf{p}(\mathbf{x})^T \mathcal{D}_j^*(\mathbf{q}^-(\mathbf{x}, t), \mathbf{x}^-, \mathbf{q}^+(\mathbf{x}, t), \mathbf{x}^+) n_j dS. \end{aligned} \quad (51)$$

Here \mathbf{p} and \mathbf{q} are the test and trial functions, and unless needed for clarity no accent is added to denote that all functions are defined over the element K . The numerical flux on the face is \mathcal{D}_j^* with the superscripts $-$ and $+$ denoting values on the two-sides of the surface, with $-$ being the inside value and $+$ the outside value; the unit normal \mathbf{n} is outward to element K .

Using the flux differencing identity (46), the DG scheme (51) can be rewritten as

$$\begin{aligned} & \int_K \mathbf{p}(\mathbf{x})^T \frac{\partial \mathbf{q}(\mathbf{x}, t)}{\partial t} d\mathbf{x} \\ &+ \sum_{j=1}^d \int_K \frac{\partial}{\partial x_j} \left(\mathbf{p}(\mathbf{y})^T \mathcal{D}_i(\mathbf{q}(\mathbf{y}, t), \mathbf{y}, \mathbf{q}(\mathbf{x}, t), \mathbf{x}) - \mathbf{p}(\mathbf{x})^T \mathcal{D}_i(\mathbf{q}(\mathbf{x}, t), \mathbf{x}, \mathbf{q}(\mathbf{y}, t), \mathbf{y}) \right) \Big|_{\mathbf{y}=\mathbf{x}} d\mathbf{x} \\ &= \int_K \mathbf{p}(\mathbf{x})^T \mathbf{g}(\mathbf{q}(\mathbf{x}, t), \mathbf{x}, t) d\mathbf{x} - \sum_{j=1}^d \int_{\partial K} \mathbf{p}(\mathbf{x})^T \mathcal{D}_j^*(\mathbf{q}^-(\mathbf{x}, t), \mathbf{x}^-, \mathbf{q}^+(\mathbf{x}, t), \mathbf{x}^+) n_j dS, \end{aligned} \quad (52)$$

where the volume and surface numerical fluxes can differ. Changing from the physical element K to the reference element \hat{K} gives the final variational form

$$\begin{aligned} & \int_{\hat{K}} J^v(\boldsymbol{\xi}) \mathbf{p}(\boldsymbol{\xi})^T \frac{\partial \mathbf{q}(\boldsymbol{\xi}, t)}{\partial t} d\hat{\mathbf{x}} \\ &+ \sum_{j,k=1}^d \int_{\hat{K}} G_{jk}(\boldsymbol{\xi}) \frac{\partial}{\partial \xi_k} \left(\mathbf{p}(\boldsymbol{\eta})^T \mathcal{D}_i(\mathbf{q}(\boldsymbol{\eta}, t), \mathbf{x}(\boldsymbol{\eta}), \mathbf{q}(\boldsymbol{\xi}, t), \mathbf{x}(\boldsymbol{\xi})) \right) \Big|_{\boldsymbol{\eta}=\boldsymbol{\xi}} d\hat{\mathbf{x}} \\ &- \sum_{j,k=1}^d \int_{\hat{K}} G_{jk}(\boldsymbol{\xi}) \frac{\partial}{\partial \xi_k} \left(\mathbf{p}(\boldsymbol{\xi})^T \mathcal{D}_i(\mathbf{q}(\boldsymbol{\xi}, t), \mathbf{x}(\boldsymbol{\xi}), \mathbf{q}(\boldsymbol{\eta}, t), \mathbf{x}(\boldsymbol{\eta})) \right) \Big|_{\boldsymbol{\eta}=\boldsymbol{\xi}} d\hat{\mathbf{x}} \\ &= \int_{\hat{K}} J^v(\boldsymbol{\xi}) \mathbf{p}(\boldsymbol{\xi})^T \mathbf{g}(\mathbf{q}(\boldsymbol{\xi}, t), \mathbf{x}(\boldsymbol{\xi}), t) d\hat{\mathbf{x}} \\ &- \sum_{j=1}^d \int_{\partial \hat{K}} J^f(\boldsymbol{\xi}) \mathbf{p}(\boldsymbol{\xi})^T \mathcal{D}_j^*(\mathbf{q}^-(\boldsymbol{\xi}, t), \mathbf{x}(\boldsymbol{\xi}^-), \mathbf{q}^+(\boldsymbol{\xi}, t), \mathbf{x}(\boldsymbol{\xi}^+)) n_j^- d\hat{S}, \end{aligned} \quad (53)$$

with $G_{jk} = J^v \frac{\partial \xi_j}{\partial x_k}$.

A quadrature-based DG semi-discretization of (53) for solution component α can be written as

$$\begin{aligned} & \mathbf{M}^v \frac{d\mathbf{q}_\alpha^N}{dt} + \mathbf{V}^T \sum_{j,k=1}^d \left(G_{jk}(\mathbf{Q}_k \circ \mathcal{D}_{j\alpha}) - (\mathcal{D}_{j\alpha} \circ \mathbf{Q}_k^T) G_{jk} \right) \mathbf{1} \\ &= (\mathbf{V}^v)^T \mathbf{J}^v \mathbf{W}^v \mathbf{g}_\alpha^v - \sum_{j,k=1}^d \left(\mathbf{V}^f \right)^T G_{jk}^f \mathbf{B}_k^f \mathcal{D}_{j\alpha}^*. \end{aligned} \quad (54)$$

Here \circ denotes the Hadamard (element-wise) product, the matrix $\mathcal{D}_{j\alpha}$ denotes component α of the numerical flux \mathcal{D}_j evaluated pairwise at the quadrature nodes with components

$$[\mathcal{D}_{j\alpha}]_{n,m} = [\mathcal{D}_j([\tilde{\mathbf{q}}]_n, [\mathbf{x}]_n, [\tilde{\mathbf{q}}]_m, [\mathbf{x}]_m)]_\alpha, \quad (55)$$

and the vector \mathbf{g}_α^v is the evaluation of the source at the volume quadrature

$$[\mathbf{g}_\alpha^v]_n = [\mathbf{g}([\tilde{\mathbf{q}}^v]_n, [\mathbf{x}^v]_n)]_\alpha. \quad (56)$$

For the element surface quadrature points, the numerical flux vector $\mathcal{D}_{j\alpha}^*$ components are

$$[\mathcal{D}_{j\alpha}^*]_n = [\mathcal{D}_j^*([\tilde{\mathbf{q}}^{-f}]_n, [\mathbf{x}^{-f}]_n, [\tilde{\mathbf{q}}^{+f}]_n, [\mathbf{x}^{+f}]_n)]_\alpha, \quad (57)$$

where the superscripts $-f$ and $+f$ refer to the inner and outer traces, respectively. Since the numeric flux is not symmetric, it will be useful later to define the numerical flux vectors $\mathcal{D}_{j\alpha}^{*-}$ and $\mathcal{D}_{j\alpha}^{*+}$ by their components as

$$[\mathcal{D}_{j\alpha}^{*-}]_n = [\mathcal{D}_{j\alpha}^*]_n, \quad [\mathcal{D}_{j\alpha}^{*+}]_n = [\mathcal{D}_j^*([\tilde{\mathbf{q}}^{+f}]_n, [\mathbf{x}^{+f}]_n, [\tilde{\mathbf{q}}^{-f}]_n, [\mathbf{x}^{-f}]_n)]_\alpha. \quad (58)$$

The vector $\tilde{\mathbf{q}}$ is defined on the combined volume and surface quadrature grid from the expansion coefficients \mathbf{q} . A natural and consistent choice is $\tilde{\mathbf{q}}_\alpha = \mathbf{V}\mathbf{q}_\alpha^N$, but as will be seen in the next section, for general element types entropy stability requires that $\tilde{\mathbf{q}}$ be defined through an entropy-projection. With the flux matrix notation (55) we have the approximation

$$\begin{aligned} \int_{\hat{K}} G_{jk}(\xi) \frac{\partial}{\partial \xi_k} \left(p_\alpha(\eta) [\mathcal{D}_j(\mathbf{q}(\eta), \mathbf{x}(\eta), \mathbf{q}(\xi), \mathbf{x}(\xi))]_\alpha \right) \Big|_{\eta=\xi} d\hat{x} \\ \approx \left(\mathbf{p}_\alpha^N \right)^T \mathbf{V}^T \mathbf{G}_{jk}(\mathbf{Q}_k \circ \mathcal{D}_{j\alpha}) \mathbf{1}, \end{aligned} \quad (59)$$

and

$$\begin{aligned} \int_{\hat{K}} G_{jk}(\xi) \frac{\partial}{\partial \xi_k} \left(p_\alpha(\xi) [\mathcal{D}_j(\mathbf{q}(\xi), \mathbf{x}(\xi), \mathbf{q}(\eta), \mathbf{x}(\eta))]_\alpha \right) \Big|_{\eta=\xi} d\hat{x} \\ \approx \left(\mathbf{p}_\alpha^N \right)^T \mathbf{V}^T \left(\mathcal{D}_{j\alpha} \circ \mathbf{Q}_k^T \right) \mathbf{G}_{jk} \mathbf{1}. \end{aligned} \quad (60)$$

Remark 1. When the quadrature and interpolation points are both Legendre–Gauss–Lobatto, i.e., the DG spectral element method, \mathbf{Q}_i can be replaced with \mathbf{Q}_i^v , the mass matrix \mathbf{M}^v is diagonal, $\mathbf{P}^v = \mathbf{V}^v = \mathbf{I}$, and \mathbf{V}^f selects points from the volume quadrature that are on the boundary.

4.5. Entropy stable DG with flux differencing in fluctuation form

By construction, DG scheme (54) is consistent, and here we discuss what is required to ensure entropy stability. Following Castro et al. [11], we assume the volume numerical flux satisfies the entropy conservation property³,

$$\boldsymbol{\beta}^T(\mathbf{p}, \mathbf{y}) \mathcal{D}_i(\mathbf{p}, \mathbf{y}, \mathbf{q}, \mathbf{x}) - \boldsymbol{\beta}^T(\mathbf{q}, \mathbf{x}) \mathcal{D}_i(\mathbf{q}, \mathbf{x}, \mathbf{p}, \mathbf{y}) = \zeta_i(\mathbf{q}, \mathbf{x}) - \zeta_i(\mathbf{p}, \mathbf{y}), \quad (61a)$$

and the surface flux the entropy dissipation property

$$\sum_{i=1}^d n_i(x) \left(\boldsymbol{\beta}^T(\mathbf{p}, \mathbf{y}) \mathcal{D}_i^*(\mathbf{p}, \mathbf{y}, \mathbf{q}, \mathbf{x}) - \boldsymbol{\beta}^T(\mathbf{q}, \mathbf{x}) \mathcal{D}_i^*(\mathbf{q}, \mathbf{x}, \mathbf{p}, \mathbf{y}) \right) \leq \sum_{i=1}^d n_i(x) (\zeta_i(\mathbf{q}, \mathbf{x}) - \zeta_i(\mathbf{p}, \mathbf{y})); \quad (61b)$$

³For conservation laws, using the numerical flux in fluctuation form (44) it is straightforward to show that (61) reduces to the standard conservative property: $(\boldsymbol{\beta}^T(\mathbf{q}, \mathbf{x}) - \boldsymbol{\beta}^T(\mathbf{p}, \mathbf{y})) \mathcal{F}_i(\mathbf{q}, \mathbf{x}, \mathbf{p}, \mathbf{y}) = \psi_i(\mathbf{q}, \mathbf{x}) - \psi_i(\mathbf{p}, \mathbf{y})$ where $\psi_i = \boldsymbol{\beta}^T \mathbf{f}_i - \zeta_i$ is the entropy potential; see Castro et al. [11].

we refer to relations (61a) and (61b) as conservative and dissipative entropy shuffle relations. For entropy stability it is critical that the numerical fluxes, source terms, and entropy variables be evaluated with a $\tilde{\mathbf{q}}$ that properly accounts for variational crimes. To do this we define the auxiliary quantities

$$\mathbf{q}_\alpha^v = \mathbf{V}^v \mathbf{q}_\alpha^N, \quad \mathbf{q}_\alpha^f = \mathbf{V}^f \mathbf{q}_\alpha^N, \quad \mathbf{q}_\alpha = \mathbf{V} \mathbf{q}_\alpha^N, \quad \alpha = 1, \dots, N_c, \quad (62a)$$

$$\mathbf{x}_i^v = \mathbf{V}^v \mathbf{x}_i^N, \quad \mathbf{x}_i^f = \mathbf{V}^f \mathbf{x}_i^N, \quad \mathbf{x}_i = \mathbf{V} \mathbf{x}_i^N, \quad i = 1, \dots, 3, \quad (62b)$$

$$(62c)$$

with the \mathbf{q}^v , \mathbf{q}^f , \mathbf{q} , \mathbf{x}^v , \mathbf{x}^f , and \mathbf{x} being the solution and coordinate vectors with all the components. The expansion coefficients of the entropy variables are defined using the quadrature L^2 projection operator (29),

$$\boldsymbol{\beta}_\alpha^N = \mathbf{P}^v \boldsymbol{\beta}_\alpha(\mathbf{q}^v, \mathbf{x}^v), \quad (63)$$

with $\boldsymbol{\beta}^N$ being the vectors of all components; we similarly define $\boldsymbol{\beta}_\alpha^v$, $\boldsymbol{\beta}_\alpha^f$, $\boldsymbol{\beta}_\alpha$, $\boldsymbol{\beta}^v$, $\boldsymbol{\beta}^f$, and $\boldsymbol{\beta}$ as above. With this, the entropy-projected solution vectors are

$$\tilde{\mathbf{q}}_\alpha^v = \boldsymbol{\beta}_\alpha^{-1}(\boldsymbol{\beta}^v, \mathbf{x}^v), \quad (64a)$$

$$\tilde{\mathbf{q}}_\alpha^f = \boldsymbol{\beta}_\alpha^{-1}(\boldsymbol{\beta}^f, \mathbf{x}^f), \quad (64b)$$

$$\tilde{\mathbf{q}}_\alpha = \boldsymbol{\beta}_\alpha^{-1}(\boldsymbol{\beta}, \mathbf{x}) = \begin{bmatrix} \tilde{\mathbf{q}}_\alpha^v \\ \tilde{\mathbf{q}}_\alpha^f \end{bmatrix}, \quad (64c)$$

with $\tilde{\mathbf{q}}^v$, $\tilde{\mathbf{q}}^f$, and $\tilde{\mathbf{q}}$ being the combined entropy-projected solution vectors.

Lemma 4. *If numerical flux \mathcal{D}_j satisfies conservative entropy shuffle (61) and $\mathcal{D}_{j\alpha}$ is evaluated with $\tilde{\mathbf{q}}$ as defined in (64) then DG scheme (54) on a single element satisfies the entropy relationship*

$$\mathbf{1}^T \mathbf{J}^v \mathbf{W}^v \frac{d\eta(\mathbf{q}^v)}{dt} \leq \mathbf{1}^T \mathbf{J}^v \mathbf{W}^v \Pi(\tilde{\mathbf{q}}^v, \mathbf{x}^v) + \sum_{j,k=1}^d \left(\mathbf{1}^T \mathbf{G}_{jk}^{+f} \mathbf{B}_k^{+f} \boldsymbol{\zeta}_j^{+f} + \sum_{\alpha=1}^{N_c} (\boldsymbol{\beta}_\alpha^{+f})^T \mathbf{G}_{jk}^{+f} \mathbf{B}_k^{+f} \mathcal{D}_{j\alpha}^{+*} \right). \quad (65)$$

PROOF. On a single element, assuming exactness in time, it follows that

$$\begin{aligned} \mathbf{1}^T \mathbf{J}^v \mathbf{W}^v \frac{d\eta(\mathbf{q}^v)}{dt} &= \sum_{\alpha=1}^{N_c} (\boldsymbol{\beta}_\alpha(\mathbf{q}^v))^T \mathbf{J}^v \mathbf{W}^v \frac{d\mathbf{q}_\alpha^v}{dt} \\ &= \sum_{\alpha=1}^{N_c} (\boldsymbol{\beta}_\alpha(\mathbf{q}^v))^T (\mathbf{P}^v)^T (\mathbf{V}^v)^T \mathbf{J}^v \mathbf{W}^v \mathbf{V}^v \frac{d\mathbf{q}_\alpha^N}{dt} \\ &= \sum_{\alpha=1}^{N_c} (\boldsymbol{\beta}_\alpha^N)^T \mathbf{M}^v \frac{d\mathbf{q}_\alpha^N}{dt}. \end{aligned} \quad (66)$$

Using DG scheme (54) then gives

$$\begin{aligned} \sum_{\alpha=1}^{N_c} (\boldsymbol{\beta}_\alpha^N)^T \mathbf{M}^v \frac{d\mathbf{q}_\alpha^N}{dt} &= - \sum_{\alpha=1}^{N_c} \sum_{j,k=1}^d \boldsymbol{\beta}_\alpha^T \left(\mathbf{G}_{jk}(\mathcal{Q}_k \circ \mathcal{D}_{j\alpha}) - (\mathcal{D}_{j\alpha} \circ \mathcal{Q}_k^T) \mathbf{G}_{jk} \right) \mathbf{1} \\ &\quad + \sum_{\alpha=1}^{N_c} (\boldsymbol{\beta}_\alpha^v)^T \mathbf{J}^v \mathbf{W}^v \mathbf{g}_\alpha^v - \sum_{\alpha=1}^{N_c} \sum_{j,k=1}^d (\boldsymbol{\beta}_\alpha^f)^T \mathbf{G}_{jk}^f \mathbf{B}_k^f \mathcal{D}_{j\alpha}^*. \end{aligned} \quad (67)$$

Considering the source term, we have that

$$\sum_{\alpha=1}^{N_c} (\boldsymbol{\beta}_\alpha^v)^T \mathbf{J}^v \mathbf{W}^v \mathbf{g}_\alpha^v = \sum_{\alpha=1}^{N_c} (\boldsymbol{\beta}_\alpha^v)^T \mathbf{J}^v \mathbf{W}^v \mathbf{g}_\alpha(\tilde{\mathbf{q}}^v, \mathbf{x}^v) = \mathbf{1}^T \mathbf{J}^v \mathbf{W}^v \Pi(\tilde{\mathbf{q}}^v, \mathbf{x}^v). \quad (68)$$

The volume flux term gives

$$\begin{aligned}
& \sum_{\alpha=1}^{N_c} \sum_{j,k=1}^d \boldsymbol{\beta}_\alpha^T \left(\mathbf{G}_{jk} (\mathbf{Q}_k \circ \mathcal{D}_{j\alpha}) - (\mathcal{D}_{j\alpha} \circ \mathbf{Q}_k^T) \mathbf{G}_{jk} \right) \mathbf{1} \\
&= \sum_{\alpha=1}^{N_c} \sum_{n,m=1}^{N_q} \sum_{j,k=1}^d [\boldsymbol{\beta}_\alpha]_n [\mathcal{D}_{j\alpha}]_{nm} \left([\mathbf{G}_{jk}]_n [\mathbf{Q}_k]_{nm} - [\mathbf{Q}_k]_{mn} [\mathbf{G}_{jk}]_m \right) \\
&= \sum_{\alpha=1}^{N_c} \sum_{n,m=1}^{N_q} \sum_{j,k=1}^d [\mathbf{G}_{jk}]_n [\mathbf{Q}_k]_{nm} \left([\boldsymbol{\beta}_\alpha]_n [\mathcal{D}_{j\alpha}]_{nm} - [\boldsymbol{\beta}_\alpha]_m [\mathcal{D}_{j\alpha}]_{mn} \right) \\
&= \sum_{n,m=1}^{N_q} \sum_{j,k=1}^d [\mathbf{G}_{jk}]_n [\mathbf{Q}_k]_{nm} \left([\zeta_j]_m - [\zeta_j]_n \right) \\
&= \sum_{j,k=1}^d \left(\mathbf{1}^T \mathbf{G}_{jk} \mathbf{Q}_k \zeta_j - \zeta_j^T \mathbf{G}_{jk} \mathbf{Q}_k \mathbf{1} \right) \\
&= \sum_{j,k=1}^d \mathbf{1}^T \mathbf{G}_{jk} \mathbf{Q}_k \zeta_j,
\end{aligned} \tag{69}$$

where we have used the entropy conservative shuffle (61a) and exactness of the derivative matrix for constants (36). Using SBP property (33) and geometric conservation law assumption (39) gives

$$\sum_{j,k=1}^d \mathbf{1}^T \mathbf{G}_{jk} \mathbf{Q}_k \zeta_j = \sum_{j,k=1}^d \left(\mathbf{1}^T \mathbf{G}_{jk}^f \mathbf{B}_k^f \zeta_j^f - \mathbf{1}^T \mathbf{G}_{jk} \mathbf{Q}_k^T \zeta_j \right) = \sum_{j,k=1}^d \mathbf{1}^T \mathbf{G}_{jk}^{-f} \mathbf{B}_k^{-f} \zeta_j^{-f}. \tag{70}$$

Now considering the face term yields

$$\begin{aligned}
& - \sum_{\alpha=1}^{N_c} \sum_{j,k=1}^d \left(\boldsymbol{\beta}_\alpha^f \right)^T \mathbf{G}_{jk}^f \mathbf{B}_k^f \mathcal{D}_{j\alpha}^* = - \sum_{\alpha=1}^{N_c} \sum_{j,k=1}^d \left(\boldsymbol{\beta}_\alpha^{-f} \right)^T \mathbf{G}_{jk}^{-f} \mathbf{B}_k^{-f} \mathcal{D}_{j\alpha}^{-*} \\
& \leq - \sum_{j,k=1}^d \left(\mathbf{1}^T \mathbf{G}_{jk}^{-f} \mathbf{B}_k^{-f} \zeta_j^{+f} - \mathbf{1}^T \mathbf{G}_{jk}^{-f} \mathbf{B}_k^{-f} \zeta_j^{-f} + \sum_{\alpha=1}^{N_c} \left(\left(\boldsymbol{\beta}_\alpha^{+f} \right)^T \mathbf{G}_{jk}^{-f} \mathbf{B}_k^{-f} \mathcal{D}_{j\alpha}^{+*} \right) \right) \\
& = \sum_{j,k=1}^d \left(\mathbf{1}^T \mathbf{G}_{jk}^{+f} \mathbf{B}_k^{+f} \zeta_j^{+f} + \mathbf{1}^T \mathbf{G}_{jk}^{-f} \mathbf{B}_k^{-f} \zeta_j^{-f} + \sum_{\alpha=1}^{N_c} \left(\left(\boldsymbol{\beta}_\alpha^{+f} \right)^T \mathbf{G}_{jk}^{+f} \mathbf{B}_k^{+f} \mathcal{D}_{j\alpha}^{+*} \right) \right),
\end{aligned} \tag{71}$$

where we have used the dissipative entropy shuffle (61b) and the fact that $\sum_{k=1}^d \mathbf{G}_{jk}^{-f} \mathbf{B}_k^{-f} = - \sum_{k=1}^d \mathbf{G}_{jk}^{+f} \mathbf{B}_k^{+f}$.

Putting the source (68), volume (70), and face (71) contributions together gives the desired result. \square

Theorem 5. *If the conditions of Lemma 4 are satisfied, then DG scheme (54) on a mesh with periodic boundary conditions satisfies the entropy stability relationship*

$$\sum_{K \in \mathcal{T}} \sum_{\alpha=1}^{N_c} \mathbf{1}^T \mathbf{J}^{v,K} \mathbf{W}^{v,K} \frac{d\eta(\mathbf{q}^{v,K})}{dt} \leq \sum_{K \in \mathcal{T}} \mathbf{1}^T \mathbf{J}^{v,K} \mathbf{W}^{v,K} \Pi(\tilde{\mathbf{q}}^{v,K}, \mathbf{x}^{v,K}), \tag{72}$$

where \mathcal{T} is the set of all elements.

PROOF. The result follows directly from the entropy shuffle (61) applied to neighboring face terms of the single element entropy relation (65) of Lemma 4.

4.6. Entropy conservative flux for the atmospheric Euler equations

For the atmospheric Euler equations (1), we construct numerical fluxes \mathcal{D}_k such that the conservative entropy shuffle (61) is satisfied. Here we use a construction based on the two-point entropy conserving flux of Chandrashekar [15] and Renac [47]. First, we define the following auxiliary quantities:

$$(\rho u_i)^* = \{\{\rho\}\}_{\log} \{\{u_i\}\}, \quad (73a)$$

$$p^* = \frac{\{\{\rho\}\}}{2\{\{b\}\}}, \quad (73b)$$

$$e^* = \frac{1}{2(\gamma-1)\{\{b\}\}_{\log}} + \{\{\phi(\mathbf{x})\}\} + \|\{\{\mathbf{u}\}\}\|_2^2 - \frac{\{\{\|\mathbf{u}\|_2^2\}\}}{2}, \quad (73c)$$

$$\hat{\rho} = \frac{\{\{b\}\}\{\{\rho\}\}_{\log}}{b^-}, \quad (73d)$$

where the average and log-average operators are defined as follows

$$\{\{a\}\} = \frac{a^+ + a^-}{2}, \quad (74a)$$

$$\{\{a\}\}_{\log} = \frac{a^+ - a^-}{\log(a^+) - \log(a^-)}. \quad (74b)$$

To evaluate $\{\{\cdot\}\}_{\log}$ in a numerically stable manner we follow the approach outlined by Ismail and Roe [31, Appendix B]. With these definitions, an entropy conservative numerical flux for $k = 1, 2, 3$ is

$$\mathcal{A}_k(\mathbf{q}^-, \mathbf{x}^-, \mathbf{q}^+, \mathbf{x}^+) = \frac{1}{2} \begin{bmatrix} 1 & 0 & 0 & 0 & 0 & 0 \\ 0 & 1 & 0 & 0 & 0 & \delta_{1k} \hat{\rho} \\ 0 & 0 & 1 & 0 & 0 & \delta_{2k} \hat{\rho} \\ 0 & 0 & 0 & 1 & 0 & \delta_{3k} \hat{\rho} \\ 0 & 0 & 0 & 0 & 1 & 0 \end{bmatrix}, \quad (75a)$$

$$\mathcal{H}_k(\mathbf{q}^-, \mathbf{x}^-, \mathbf{q}^+, \mathbf{x}^+) = \begin{bmatrix} (\rho u_k)^* \\ (\rho u_k)^* \{\{u_1\}\} + \delta_{1k} p^* \\ (\rho u_k)^* \{\{u_2\}\} + \delta_{2k} p^* \\ (\rho u_k)^* \{\{u_3\}\} + \delta_{3k} p^* \\ e^* (\rho u_k)^* + \{\{u_k\}\} p^* \\ \phi(\mathbf{x}^+) \end{bmatrix}. \quad (75b)$$

Using these expressions in the definition of the numerical flux (41) gives

$$\mathcal{D}_k(\mathbf{q}^-, \mathbf{x}^-, \mathbf{q}^+, \mathbf{x}^+) = \begin{bmatrix} (\rho u_k)^* \\ (\rho u_k)^* \{\{u_1\}\} + \delta_{1k} \left(p^* + \frac{1}{2} \hat{\rho} [[\phi]] \right) \\ (\rho u_k)^* \{\{u_2\}\} + \delta_{2k} \left(p^* + \frac{1}{2} \hat{\rho} [[\phi]] \right) \\ (\rho u_k)^* \{\{u_3\}\} + \delta_{3k} \left(p^* + \frac{1}{2} \hat{\rho} [[\phi]] \right) \\ e^* (\rho u_k)^* + \{\{u_k\}\} p^* \end{bmatrix} - \begin{bmatrix} \rho^- u_k^- \\ \rho^- u_k^- u_1^- + \delta_{1k} p^- \\ \rho^- u_k^- u_2^- + \delta_{2k} p^- \\ \rho^- u_k^- u_3^- + \delta_{3k} p^- \\ \rho^- e^- u_k^- + u_k^- p^- \end{bmatrix}, \quad (76)$$

where $[[\phi]] = \phi(\mathbf{x}^+) - \phi(\mathbf{x}^-)$.

Since the second term of (76) is independent of \mathbf{q}^+ , it need not be included in either the volume or surface numerical fluxes. To see this, first notice that for any matrix with identical columns $\mathbf{A} = \mathbf{a} \mathbf{1}^T$ and arbitrary matrix \mathbf{B} we have $(\mathbf{A} \circ \mathbf{B}) \mathbf{1} = \mathbf{a} \circ (\mathbf{B} \mathbf{1})$. Let us denote the part of the numerical flux matrix that is independent of the second argument by $\mathcal{D}_{j\alpha}^0 = \mathbf{d}_{j\alpha}^0 \mathbf{1}^T$. Using the aforementioned property in the first derivative term of DG scheme (54) gives

$$\mathbf{v}^T \sum_{j,k=1}^d \left(\mathbf{G}_{jk} (\mathcal{Q}_k \circ \mathcal{D}_{j\alpha}^0) \right) \mathbf{1} = \mathbf{v}^T \sum_{j,k=1}^d \mathbf{G}_{jk} \mathbf{d}_{j\alpha}^0 \circ (\mathcal{Q}_k \mathbf{1}) = \mathbf{0}, \quad (77)$$

because \mathbf{Q}_k is exact for constants. In the derivative term that comes second we use the SBP property of \mathbf{Q}_k to get

$$- \mathbf{V}^T \sum_{j,k=1}^d \left(\left(\mathcal{D}_{j\alpha}^0 \circ \left(-\mathbf{Q}_k + \begin{bmatrix} \mathbf{0} \\ \mathbf{B}_i^f \end{bmatrix} \right) \mathbf{G}_{jk} \right) \right) \mathbf{1}. \quad (78)$$

Using the special form of $\mathcal{D}_{j\alpha}^0$ the first term expands to $\mathbf{V}^T \sum_{j,k=1}^d \left(d_{j\alpha}^0 \circ (\mathbf{Q}_k \mathbf{G}_{jk} \mathbf{1}) \right) = \mathbf{0}$, because of geometric conservation law (39). In the second term the boundary matrix selects $-(\mathbf{V}^f)^T \sum_{j,k=1}^d \left(\mathbf{G}_{jk}^f \mathbf{B}_k^f \mathcal{D}_{j\alpha}^{0*} \right)$, which cancels with the identical contribution coming from the surface term on the right hand side of (54).

Entropy-stable fluxes can be constructed by adding entropy dissipation terms to the entropy conservative flux in a number of ways, the simplest being local Lax-Friedrichs (Rusanov) dissipation [44, Section 6.1]. In Appendix A an entropy dissipative flux using a matrix dissipation term is described following the methodology presented in Winters et al. [64]. The matrix dissipation term improves upon scalar dissipation by distinguishing between advective and acoustic waves using the flux Jacobian eigendecomposition.

5. Numerical results

In this section, numerical results verifying correctness and highlighting the benefits of the novel entropy-stable scheme are presented. A one-dimensional Sod problem under gravity showcases the flexibility of the method in terms of different possible choices of quadrature points, while demonstrating stability in the presence of shocks. A classical atmospheric benchmark of a thermal bubble convection is used to numerically validate entropy conservation and highlight the benefits of the high-order DG scheme with numerical flux dissipation for a large eddy simulation scale flow with sharp gradients and small-scale features. A gravity wave test case in a channel, having an exact linear solution, verifies convergence and the high-order accuracy of the scheme. Lastly, a baroclinic wave benchmark demonstrates the robustness of high-order entropy stable numerics for an archetype of global weather simulation on anisotropic spherical grids. Unless otherwise noted, the surface flux used in the test problems is the entropy dissipative flux from Appendix A; in all cases the entropy conservative numerical flux (41) is used in the volume. In all examples, the Courant–Friedrichs–Lewy (CFL) number is defined with respect to the minimum distance between interpolation points and an estimate of the acoustic wave speed based on the test case initial condition.

5.1. Sod shock tube with gravity

Luo et al. [39] introduced a classical Sod shock tube placed in a gravitational field. The domain is $[0, 1]$, the geopotential $\phi = x$, and the initial condition is defined as follows

$$(\rho, u, p) = \begin{cases} (1, 0, 0) & x < 0.5, \\ (0.125, 0, 0.1) & x \geq 0.5. \end{cases} \quad (79)$$

Entropy stable no-flux boundary conditions are used on both sides of the domain [54]. The domain is resolved using 32 elements with polynomial order 4. Time integration is performed using the fourth-order five-stage low storage Runge–Kutta (LSRK54) method from Carpenter and Kennedy [10,(5,4) 2N-Storage RK scheme, solution 3] with CFL = 0.2. To assess the impact of quadrature rule accuracy, simulations using two sets of quadrature points are considered: $N + 1$ Legendre–Gauss–Lobatto (LGL) points and a more accurate $N + 2$ point Gauss quadrature. Figure 1 and Figure 2 show the density, velocity, total energy, and pressure fields at time $t = 0.2$ for the LGL and Gauss point simulations, respectively, along with a reference simulation that uses a 5th order WENO scheme with 2000 cells. The results suggest that for this test problem, there is no significant improvement with more accurate Gauss quadrature.

5.2. Rising thermal bubble

To verify the entropy conservation and entropy stability of the discretization we consider the classic atmospheric benchmark of thermal convection. Our compressible setup closely follows the anelastic experiments presented in Smolarkiewicz and Pudykiewicz [52]. A buoyant bubble is placed in a neutrally stratified environment with potential temperature 300 K. The domain $(-\frac{L}{2}, \frac{L}{2}) \times (0, H)$ with $(L, H) = (2 \text{ km}, 2 \text{ km})$ is periodic in the horizontal with rigid-lid

LGL(N+1)

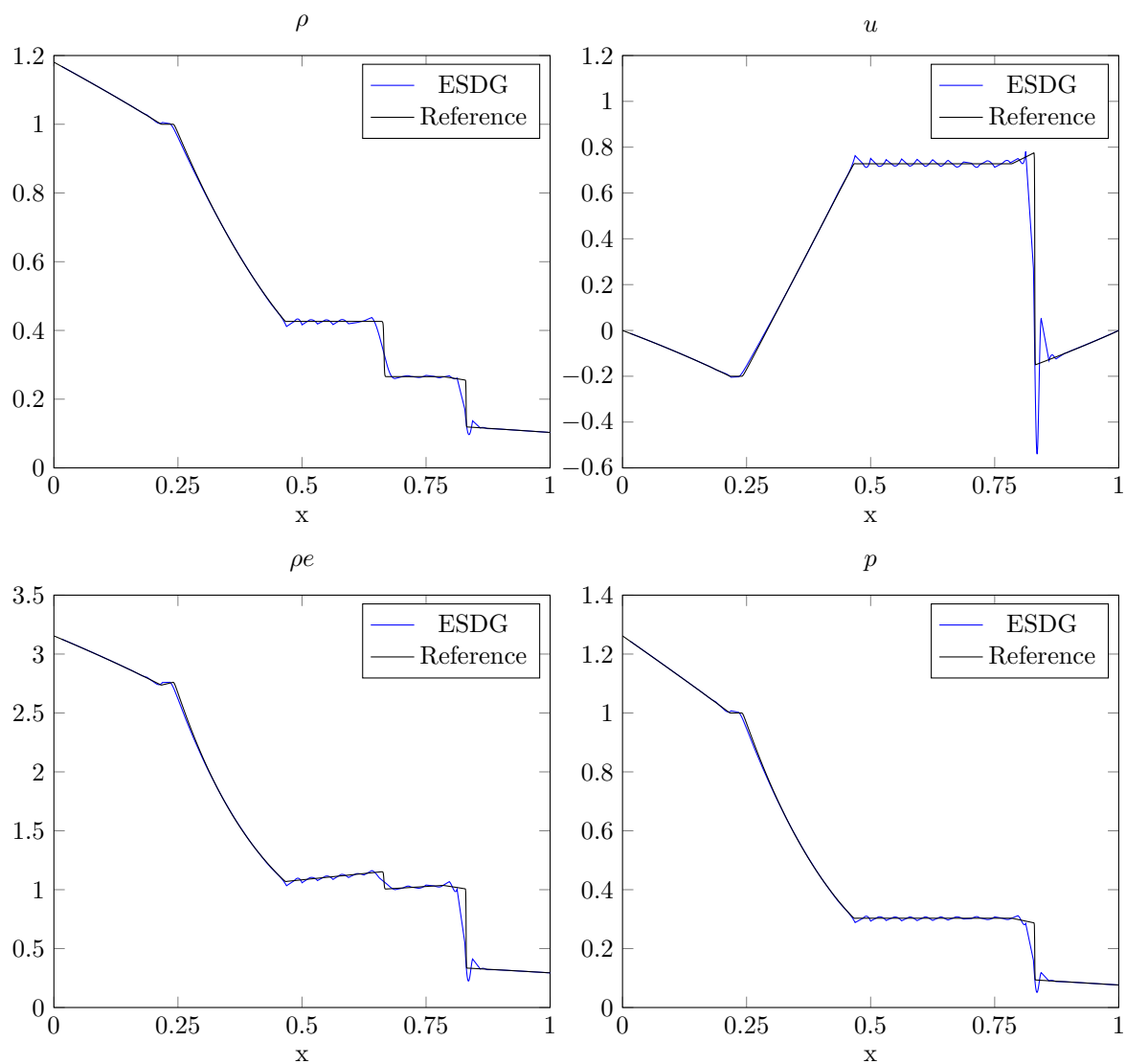


Figure 1: Density, velocity, total energy, and pressure at time $t = 0.2$ for the Sod shock tube under gravity. The solution is obtained on a grid with 32 elements with polynomial order $N = 4$ using an $N + 1$ point LGL quadrature rule. The reference results were obtained using a 5th order WENO scheme with 2000 cells.

GQ(N+2)

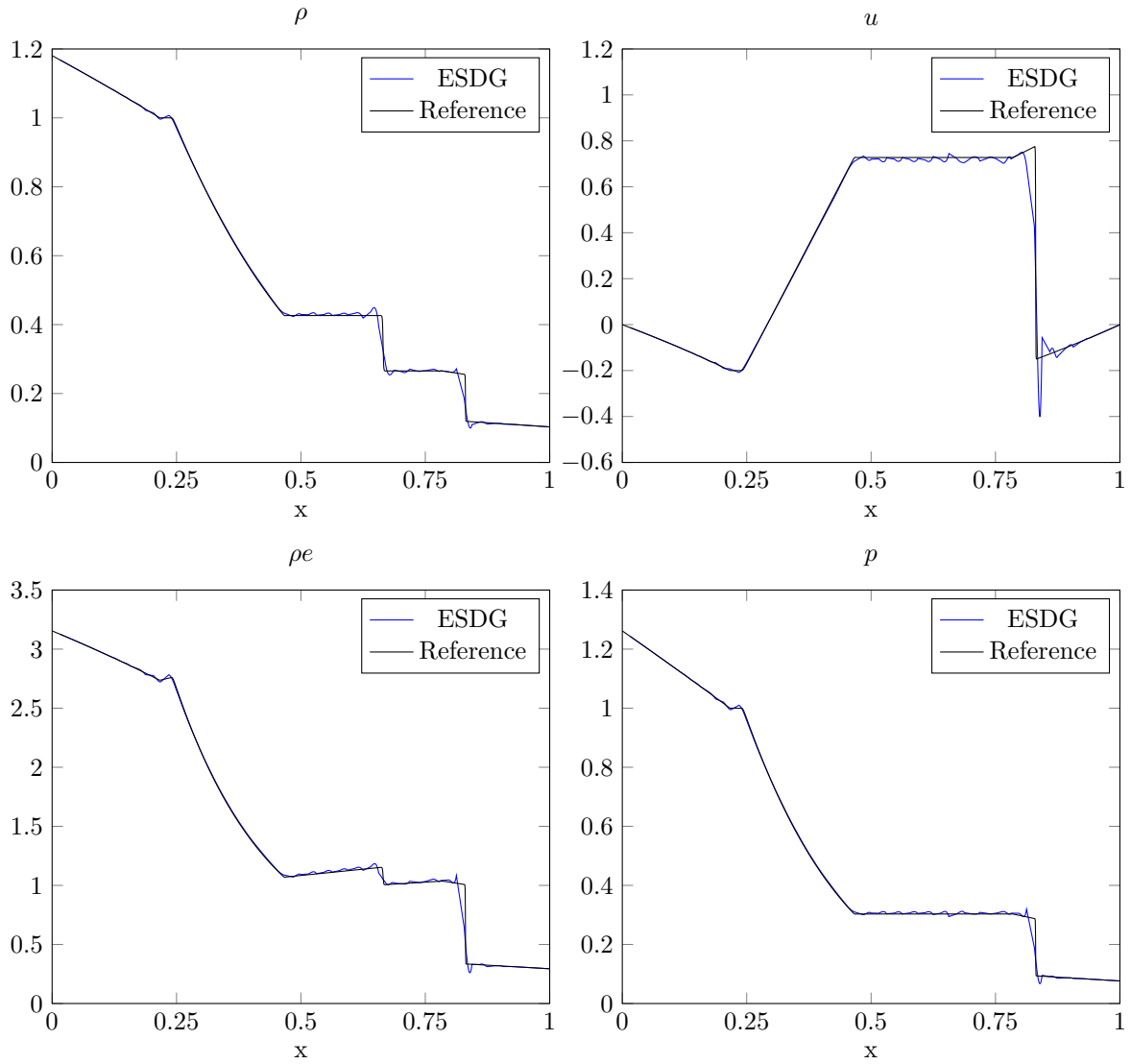


Figure 2: Density, velocity, total energy, and pressure at time $t = 0.2$ for the Sod shock tube under gravity. The solution is obtained on a grid with 32 elements with polynomial order $N = 4$ using an $N + 2$ point Gauss quadrature rule. The reference results were obtained using a 5th order WENO scheme with 2000 cells.

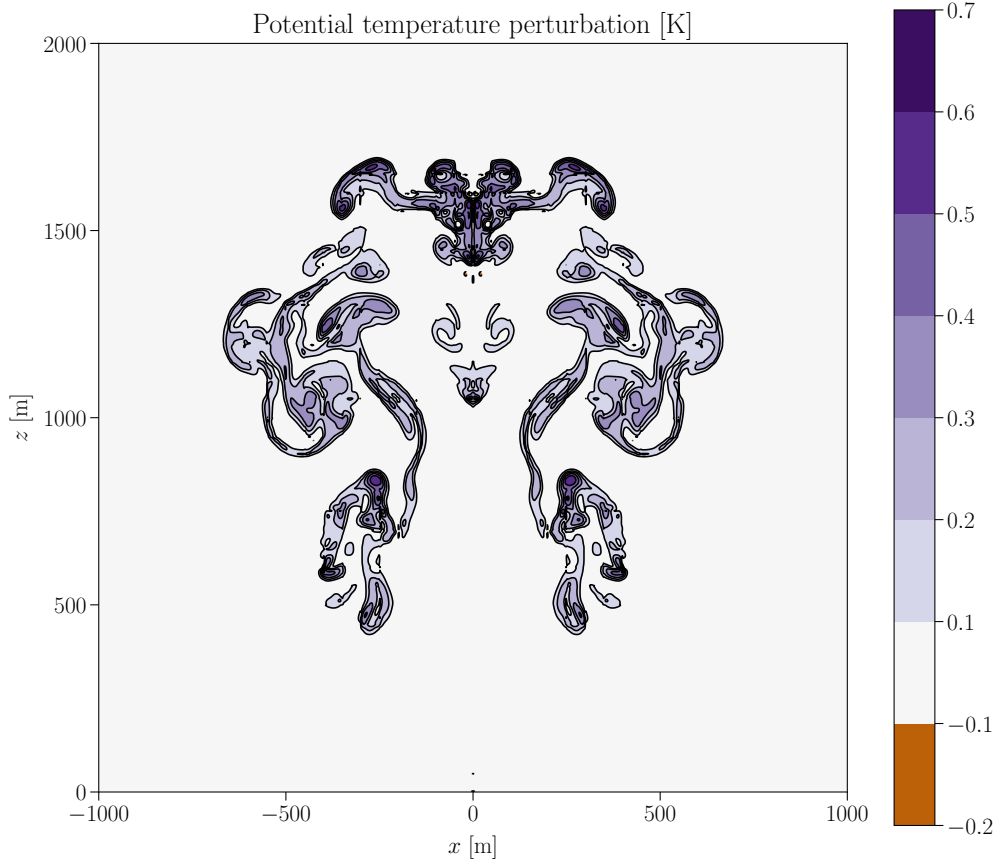


Figure 3: Potential temperature perturbation for the rising thermal bubble test case using the matrix dissipation flux at time 1000 s on a fine mesh.

boundaries at the top and bottom. The initial perturbation is a thermal bubble of radius 250 m with its center 260 m above the bottom and a potential temperature constant value of 0.5 K. The domain is resolved using $K \times K$ elements with polynomial order $N = 4$. Here, and in the subsequent examples, only the $N + 1$ point LGL quadrature rule is considered. Since the aim of this test is to verify the entropy conservation and stability properties of the scheme, we augment the LSRK54 scheme with the relaxation technique from Ranocha et al. [46]. The CFL number is 0.4.

Figure 3 shows the potential temperature perturbation at time 1000 s computed using the entropy stable flux on a fine mesh with $K = 40$ elements. Since the scheme has minimal dissipation through the matrix flux, the solution is rich in small-scale structures a feature that would not be possible with other stabilization mechanisms at this resolution.

Figure 5 shows the normalized entropy change over time for the rising thermal bubble using both the entropy conservative and entropy dissipative surface fluxes. To challenge the scheme, a coarser mesh with $K = 10$ elements is used and the mesh is warped by the transformation

$$\tilde{x}_1 = x_1 + \frac{L}{5} \sin \frac{\pi(x_1 + \frac{L}{2})}{L} \sin \frac{2\pi x_2}{H}, \quad (80)$$

$$\tilde{x}_2 = x_2 - \frac{H}{5} \sin \frac{2\pi(x_1 + \frac{L}{2})}{L} \sin \frac{\pi x_2}{H}. \quad (81)$$

This mesh warping is illustrated in Figure 4. As expected, the simulation using the entropy conservative flux conserves entropy to machine precision, while the simulation with the entropy stable flux shows strict entropy decay. Also shown

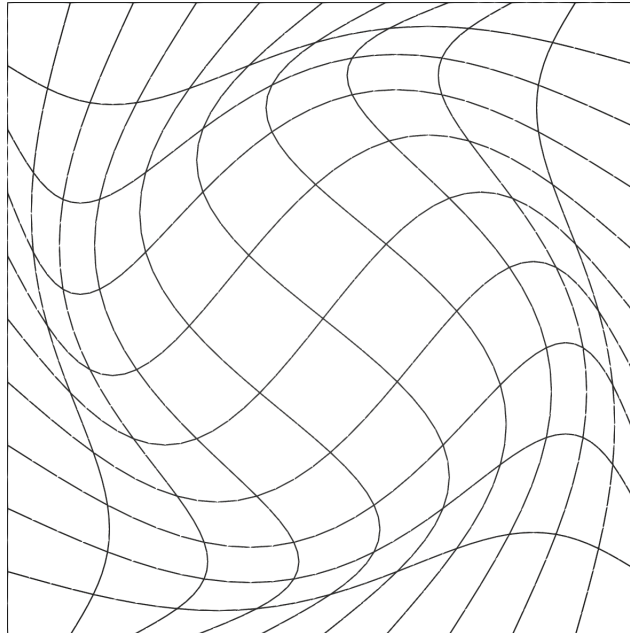


Figure 4: Warped curvilinear mesh used in the rising thermal bubble simulations verifying entropy conservation and entropy stability.

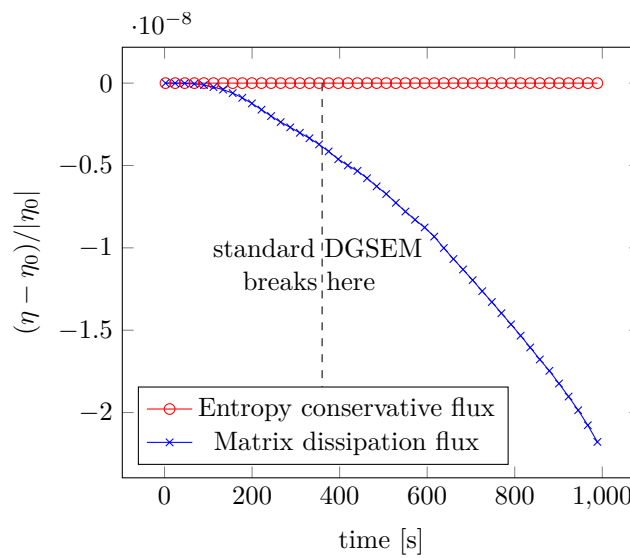


Figure 5: Time evolution of normalized entropy change for the rising thermal bubble simulations using entropy conservative and entropy stable fluxes on a coarse warped mesh. With the entropy conservative flux the maximum value of entropy change is less than 2.6×10^{-15} .

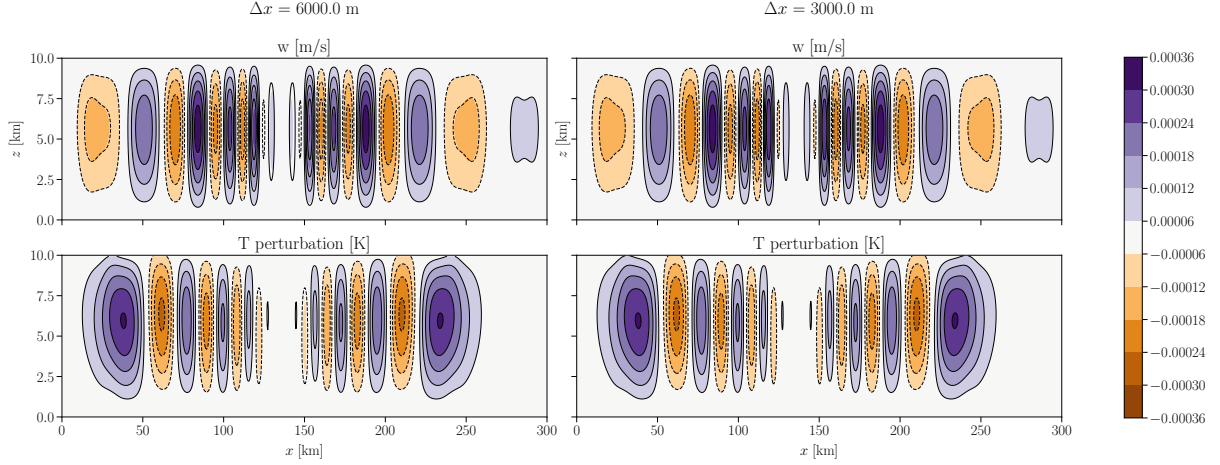


Figure 6: Temperature perturbation and vertical velocity for the gravity wave test case at time 30 min for grids with horizontal element sizes $\Delta x = 6$ km and $\Delta x = 3$ km. The contours present the analytical results whereas shading corresponds to the numerical solution.

in Figure 5 is a line denoting where the standard DG spectral element simulation with a Rusanov flux and no other stabilization method crashes with a NaN error.

5.3. Gravity wave in a channel

To verify the high-order convergence of the entropy-stable scheme, a gravity wave test case from Baldauf and Brdar [4] was adopted. The two-dimensional setup specifies a channel of size $L \times H$ with $L = 300$ km and $H = 10$ km. The boundary conditions are periodic in the horizontal and no-flux in the vertical. The geopotential is $\phi = gz$ where $g = 9.81$ m/s² and z is the vertical coordinate. An isothermal background state with temperature $T_0 = 250$ K is perturbed by a warm bubble with a maximum temperature perturbation ΔT triggering the evolution of gravity and acoustic waves. A uniform background flow of speed 20 m/s and no Coriolis force is assumed. An exact solution of the linearized problem is available, which can also be used to verify the convergence of models solving the full nonlinear equations, provided the initial perturbation is small enough [4]. Since the solution is obtained by complex trigonometric series expansion, we do not repeat it here, but refer the reader to Section 2 in Baldauf and Brdar [4] for the analytical solution and to Section 3.1 for the parameters of their “small-scale setup”. Experience from Blaise et al. [7] and Baldauf [3], which used this test case to evaluate high-order DG solvers, shows that for high orders of accuracy ΔT has to be very small to avoid error saturation due to nonlinear effects. Following Baldauf [3], we deviate from the canonical setup in Baldauf and Brdar [4] by decreasing ΔT to 10^{-3} K.

The channel is discretized by a uniform grid with $K_h \times K_v$ elements. In all simulations the ratio between the horizontal element size $\Delta x = \frac{L}{K_h}$ and the vertical element size $\Delta z = \frac{H}{K_v}$ is held constant $\frac{\Delta x}{\Delta z} = 3$. Time integration is done using the LSRK54 time stepper with CFL = 0.1.

Figure 6 presents temperature and vertical velocity perturbations at the final simulation time 30 min using polynomial order $N = 3$ for coarse and fine grids with $\Delta x = 6$ km and $\Delta x = 3$ km, respectively. The contours present the analytical results whereas shading corresponds to the numerical solution. Small differences between the numerical and analytical solutions can be observed on the coarse grid, whereas the two are nearly indistinguishable on the fine grid. This is further corroborated by Figure 7 which shows the numerical and analytical vertical velocity perturbation at $z = 5$ km for the two grids. The vertical velocity perturbation for $\Delta x = 3$ km in Figure 6 can be directly compared to Figure 2 in Baldauf [3]. With the same polynomial order and resolution our entropy-stable DG scheme is clearly more accurate, which may be surprising since Baldauf [3] used more accurate Gauss quadrature. The main reason for this is that, as proven in Appendix B, the entropy stable scheme is well-balanced for isothermal atmospheres. It is well known that well-balanced schemes are better at approximating small perturbations around balanced states [12], which is exactly the situation in this test problem. Figure 8 shows convergence in the normalized L_2 error norm for the temperature and

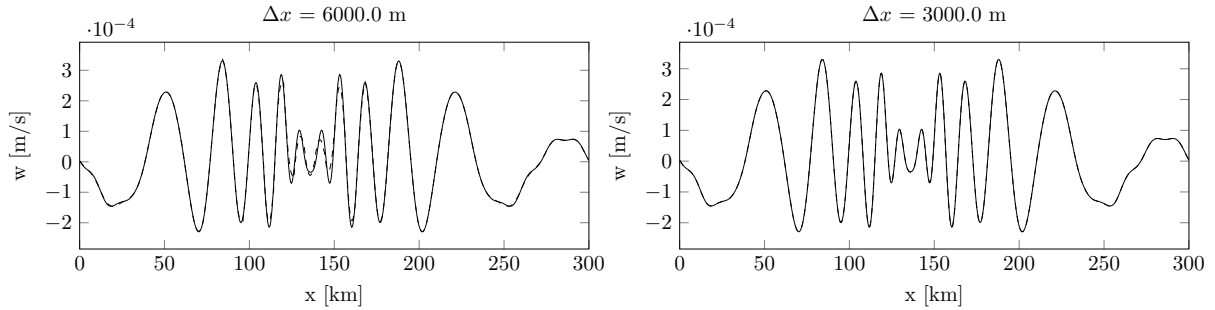


Figure 7: Vertical velocity at 5 km height for the gravity wave test case at time 30 min for grids with horizontal element sizes $\Delta x = 6$ km and $\Delta x = 3$ km. The dashed line shows the simulation results whereas the solid line shows the linear analytic solution.

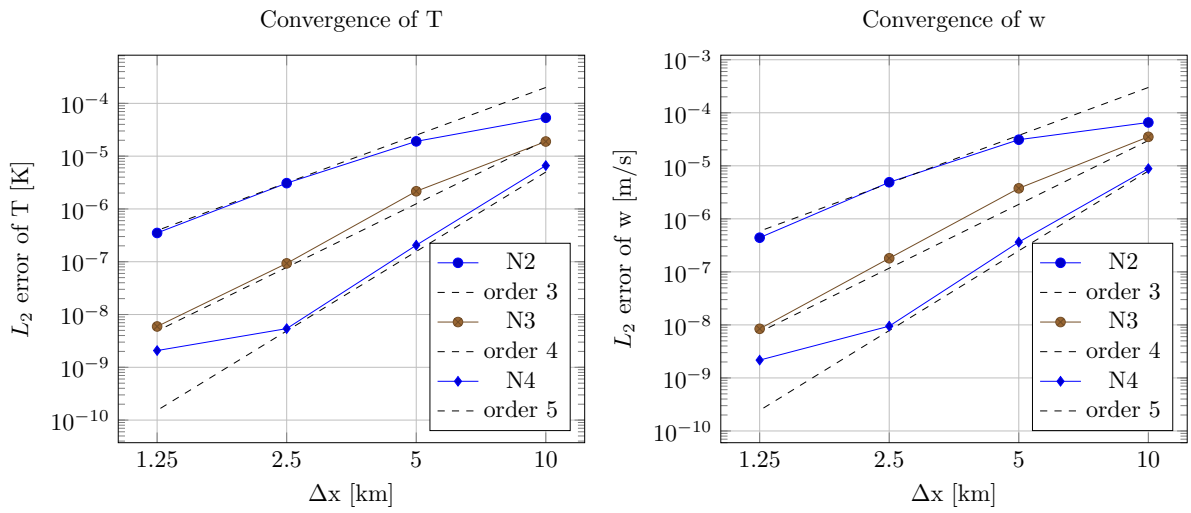


Figure 8: Convergence of temperature (left) and vertical velocity (right) errors under grid refinement for the gravity wave test case in the L_2 norm for polynomial orders 2, 3, and 4 on unwarped meshes. Dashed lines indicate orders 3, 4, and 5 convergence; the break-down of convergence when the L^2 is less than 10^{-8} is also seen in Baldauf [3].

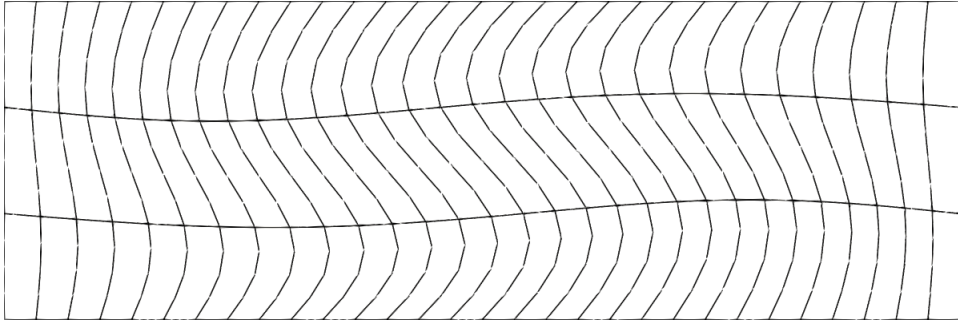


Figure 9: An example of warped mesh used to check convergence on curvilinear meshes in the gravity wave experiment. For visualization purposes the plotted mesh is enlarged by a factor of 10 in the vertical direction.

vertical velocity. The L_2 error norm is computed as

$$L_2(q) = \sqrt{\frac{\int (q - q_{exact})^2 dx}{LH}}. \quad (82)$$

Overall, we observe convergence rates close to the expected $N + 1$ for approximation with polynomial order N . When compared to Figure 3 in Baldauf [3] we see much smaller errors of the entropy-stable scheme at coarse resolutions, which is explained by its well-balanced property. Similarly as Baldauf [3], we see a small influence of nonlinear effects for the highest polynomial order $N = 4$, leading to suboptimal convergence near the finest resolution. To verify high-order accuracy of our scheme on curvilinear meshes, we repeat the convergence experiment on a sequence of meshes warped by the transformation

$$\tilde{x}_1 = x_1 + \frac{L}{20} \sin \frac{\pi(x_1)}{L} \sin \frac{2\pi x_2}{H}, \quad (83)$$

$$\tilde{x}_2 = x_2 - \frac{H}{20} \sin \frac{2\pi(x_1)}{L} \sin \frac{\pi x_2}{H}. \quad (84)$$

An example of a mesh warped by this transformation is shown in Figure 9. The convergence results are presented on Figure 10. Since the scheme is not well-balanced on curved meshes, the magnitude of errors is much larger on coarse meshes than without warping. While some of the convergence curves are not as close to the ideal $N + 1$ convergence rate as in the unwarped case, overall the scheme achieves increased order of accuracy with increased polynomial order. The convergence rate for the vertical velocity appears even higher than $N + 1$ for polynomial orders 3 and 4.

5.4. Baroclinic instability

Here, we set up a standard benchmark for atmospheric models in a spherical configuration, used to compare dynamical cores within the 2016 edition of DCMIP (Dynamical Core Intercomparison Project) [59], following the description in Ullrich et al. [60]. The test case is designed to idealize global weather evolution in the midlatitudes. The model is initialized with a deep-atmosphere, balanced steady-state solution that is axisymmetric about the Earth's rotation axis, summarized in appendix A of Ullrich et al. [60]. The geopotential is $\phi = gr$ where r is the radial distance from the center of the sphere with $g = 9.80616 \text{ m/s}^2$ and the planetary rotation vector is $\omega = (0, 0, 2\Omega)$ with $\Omega = 7.29212 \times 10^{-5} \frac{1}{s}$. A localized Gaussian hill perturbation of the zonal wind field is introduced in the northern midlatitudes, which triggers the evolution of a baroclinic wave over the course of several days. The analytical description of the triggering mechanism can be found in Section 6 of Ullrich et al. [60]. In the initial 7-day period, the wave dynamics is linear, after which the dynamics transitions to a nonlinear regime with a steepening and breaking of the wave. To compare with other models, in our presentation the focus is on the first 15 days, and particularly day 8 (before the wave breaking) and day 10 (after the wave breaking). However, to properly evaluate the robustness of the entropy-stable scheme, we confirmed that all our simulations successfully run for over 100 days without any explicit dissipation. To resolve the sphere, we use an equiangular cubed-sphere mesh with K_h elements per horizontal side on each of the six panels and K_v elements in the vertical. The model top is 30 km and rigid lid boundary conditions are

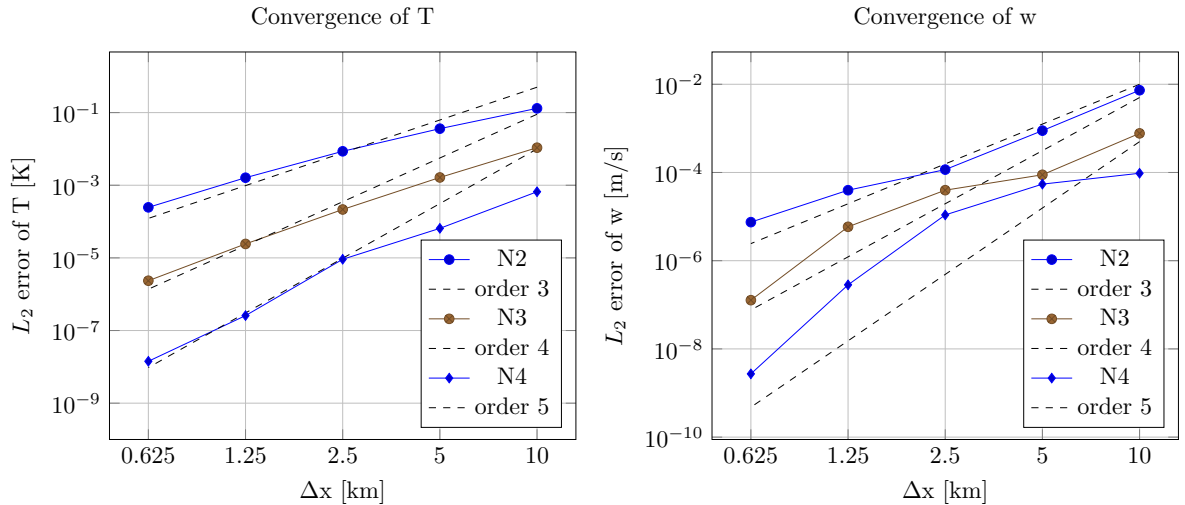


Figure 10: Convergence of temperature (left) and vertical velocity (right) errors under grid refinement for the gravity wave test case in the L_2 norm for polynomial orders 2, 3, and 4 on warped meshes. Dashed lines indicate orders 3, 4, and 5 convergence.

assumed at the top and bottom. We perform two simulations with polynomial orders 3 and 7. The simulation with polynomial order 3 uses $K_h = 30$ and $K_v = 8$, while the simulation using polynomial order 7 uses $K_h = 15$ and $K_v = 4$. These choices ensure that the total number of degrees of freedom is the same for both simulations, corresponding to about 100 km average horizontal resolution and 32 vertical levels. For time stepping we use an implicit-explicit formulation, where terms related to the vertical dynamics were treated implicitly in a linear fashion. Following Giraldo et al. [28], the splitting is achieved by subtracting a linearization of (1) from the full equations and then adding it back in; see (3.2) in Giraldo et al. [28]. The linearized equations are discretized using a standard (non entropy stable) DG method based on the same polynomial order and quadrature rule as the entropy stable discretization. To integrate the split equations in time, the second order additive Runge Kutta scheme from Giraldo et al. [28] was used with CFL = 3.0.

Figure 11 and Figure 12 show plots of surface pressure, 850 hPa temperature and relative vorticity at days 8 and 10 for polynomial orders 3 and 7, respectively. These results can be directly compared to results from the MCore and ENDGame models [60, Figures 4 and 5] and the MPAS model [51, Figure 2]. The pressure and temperature fields in their overall structure look smooth and compare very well with other models, showing only small amounts of grid-scale oscillations due to minimal numerical diffusion of our method. More noise can be seen in the relative vorticity fields, especially with polynomial order 7. This is consistent with Skamarock et al. [51], which found that the relative vorticity field is more sensitive to numerical dissipation than the pressure and temperature fields.

Figure 13 shows the time evolution of the minimum surface pressure and maximum horizontal velocity for both polynomial orders, and can be compared to results from the MPAS model in Skamarock et al. [51, Figures 3 and 4]. The surface pressure evolution is close for both polynomial orders up until day 12 and compares well to other models. The maximum horizontal speed shows consistently higher maxima for polynomial order 7. This further confirms that the higher order simulation introduces less numerical dissipation. The presented results successfully demonstrate that the new entropy-stable scheme is robust and provides high-quality solutions using only numerical flux dissipation for very high orders of accuracy in atmospheric simulations. For realistic applications, e.g., climate simulations and weather prediction, it might be beneficial to add more dissipation to damp grid-scale oscillations; an advantage of the entropy-stable scheme is that any additional regularization can be guided solely by the needs of the model physics since the dynamics is provably stable.

6. Concluding Remarks

We have extended the work of Renac [47] to develop a flux differencing formulation of the DG method for non-conservative balance laws on elements that have operators that can be skew-hybridized [14]. By specifying the

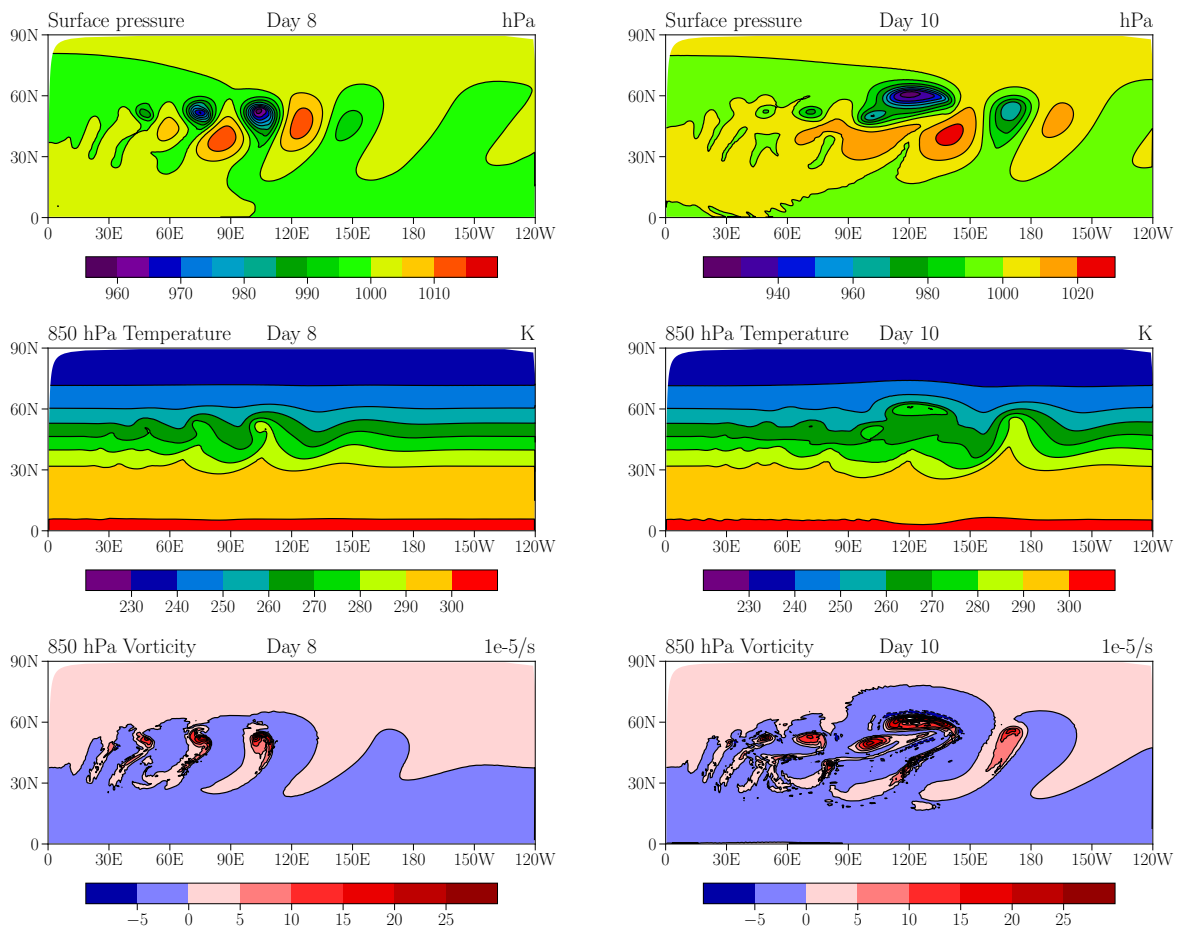


Figure 11: Results for the baroclinic wave benchmark using polynomial order 3 at day 8 (left) and 10 (right). Top to bottom: surface pressure, temperature at 850 hPa, and relative vorticity at 850 hPa.

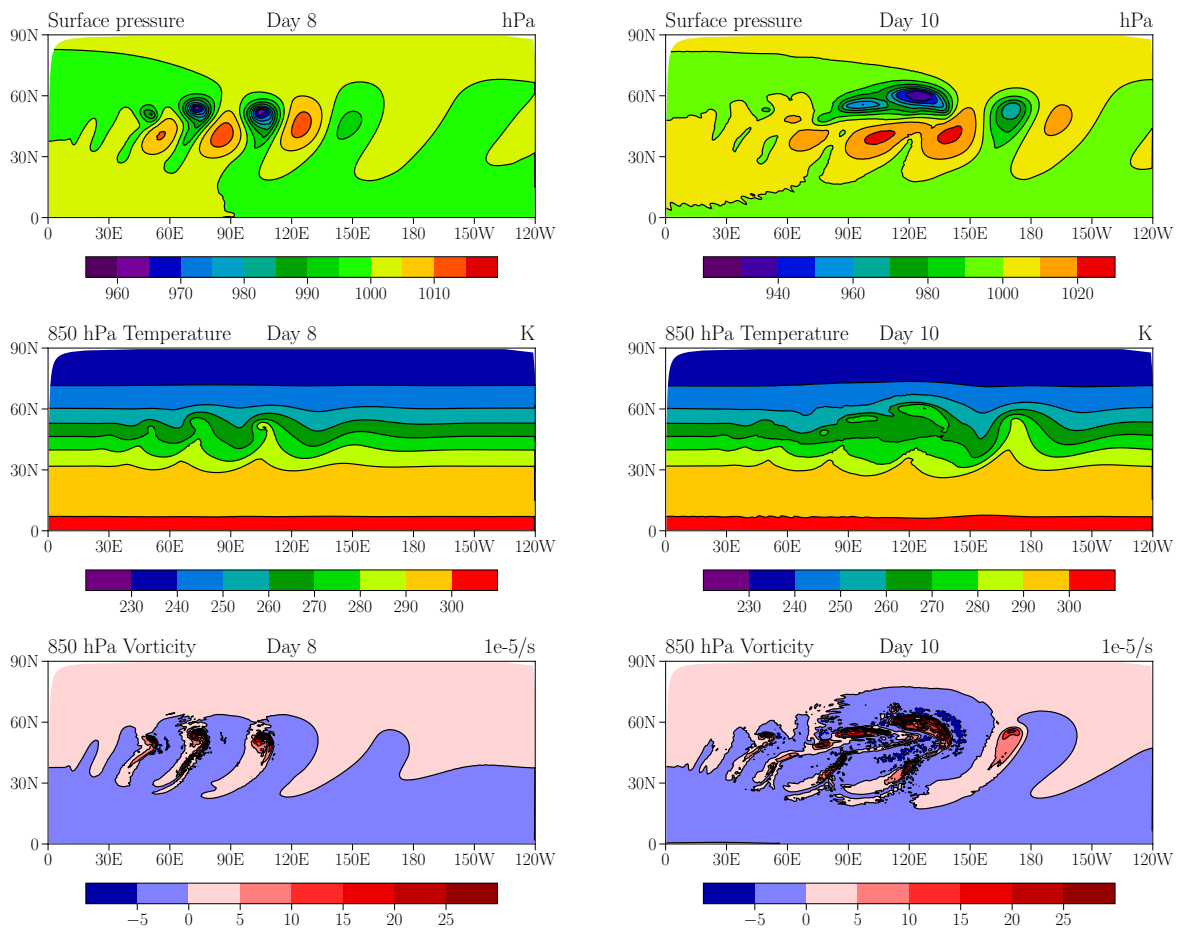


Figure 12: Results for the baroclinic wave benchmark using polynomial order 7 at day 8 (left) and 10 (right). Top to bottom: surface pressure, temperature at 850 hPa, and relative vorticity at 850 hPa.

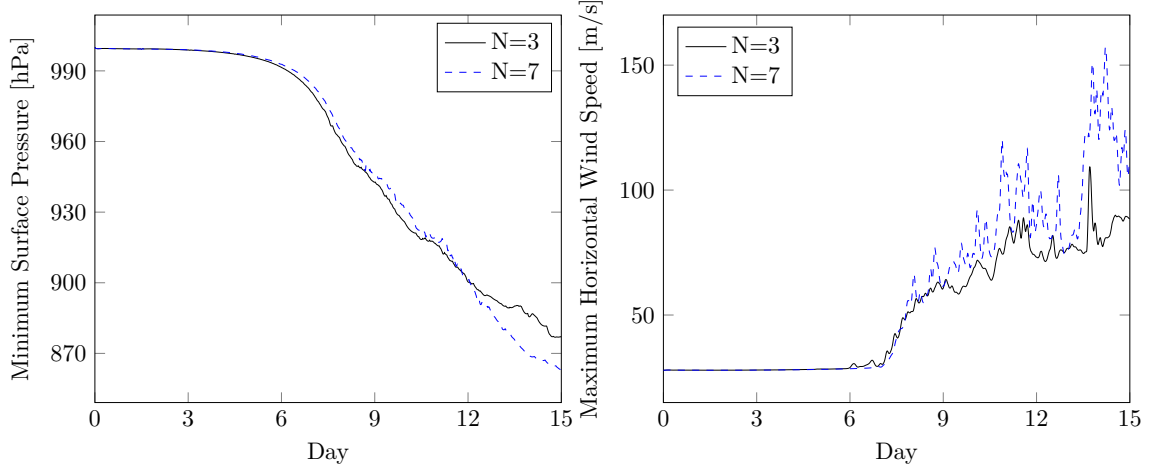


Figure 13: Time evolution of the minimum surface pressure (left) and maximum horizontal wind speed (right) for the baroclinic wave benchmark using polynomial orders 3 and 7.

volume and surface numerical fluxes so that they satisfy an additional entropy conservation and dissipation relation, the scheme was proved to be entropy stable. Based on the new framework, an entropy-stable DG discretization of the Euler equations with gravity has been constructed. Entropy-conservative and entropy-stable numerical fluxes for the Euler equations with gravity have been given in explicit form. The entropy stability and high-order accuracy of the novel scheme have been verified on standard atmospheric benchmark problems. As the atmospheric test problems show, the scheme is quite robust even without any explicit stabilization techniques beyond the choice of numerical fluxes.

Acknowledgements

Waruszewski, Kozdon, Wilcox, and Giraldo were supported by the generosity of Eric and Wendy Schmidt by recommendation of the Schmidt Futures program. Waruszewski, Kozdon, Wilcox, Gibson, and Giraldo were supported by the National Science Foundation under grant AGS-1835881. Giraldo was also supported by Office of Naval Research under grant N0001419WX00721.

Data availability statement

The code to generate, analyze, and plot the datasets used in this study can be found in the associated reproducibility repository <https://github.com/mwarusz/paper-esdg-nonconservative-gravity>.

Appendix A. Entropy stable flux with matrix dissipation

To construct an entropy stable flux the normal entropy conservative flux $\mathcal{D}_n = n_1 \mathcal{D}_1 + n_2 \mathcal{D}_2 + n_3 \mathcal{D}_3$ is combined with a dissipation operator \mathbf{H}_n acting on the jump in entropy variables, leading to the normal entropy stable flux

$$\mathcal{D}_n^* = \mathcal{D}_n - \frac{1}{2} \mathbf{H}_n [[\beta]]. \quad (\text{A.1})$$

To ensure entropy dissipation and stability, the operator \mathbf{H}_n has to be constructed carefully [20]. Here, motivated by Winters et al. [64], the dissipation operator is constructed in the so-called “matrix” form

$$\mathbf{H}_n = \mathbf{R}_n^T |\Lambda_n| \mathbf{T}_n \mathbf{R}_n, \quad (\text{A.2})$$

where \mathbf{R}_n is the matrix of right eigenvectors of the normal flux Jacobian, $|\mathbf{\Lambda}_n|$ is the corresponding matrix of absolute eigenvalues, and T_n is a scaling matrix. These matrices are given explicitly as

$$\mathbf{R}_n = \begin{bmatrix} 1 & 1 & 0 & 0 & 1 \\ \{\{u_1\}\} - c^*n_1 & \{\{u_1\}\} & m_1 & \ell_1 & \{\{u_1\}\} + c^*n_1 \\ \{\{u_2\}\} - c^*n_2 & \{\{u_2\}\} & m_2 & \ell_2 & \{\{u_2\}\} + c^*n_2 \\ \{\{u_3\}\} - c^*n_3 & \{\{u_3\}\} & m_3 & \ell_3 & \{\{u_3\}\} + c^*n_3 \\ h^* - u_n c^* & \frac{\overline{u^2}}{2} + \{\{\phi\}\} & \mathbf{m} \cdot \{\{\mathbf{u}\}\} & \boldsymbol{\ell} \cdot \{\{\mathbf{u}\}\} & h^* + u_n c^* \end{bmatrix}, \quad (\text{A.3})$$

$$|\mathbf{\Lambda}_n| = \text{diag}(|u_n - c^*|, |u_n|, |u_n|, |u_n|, |u_n + c^*|), \quad (\text{A.4})$$

$$\mathbf{T}_n = \text{diag}\left(\frac{\{\{\rho\}\}_{\log}}{2\gamma}, \frac{(\gamma - 1)\{\{\rho\}\}_{\log}}{\gamma}, p^*, p^*, \frac{\{\{\rho\}\}_{\log}}{2\gamma}\right), \quad (\text{A.5})$$

where

$$u_n = \mathbf{n} \cdot \{\{\mathbf{u}\}\}, \quad (\text{A.6})$$

$$\overline{u^2} = 2\|\{\{\mathbf{u}\}\}\|_2^2 - \{\{\|\mathbf{u}\|_2^2\}\}, \quad (\text{A.7})$$

$$p^* = \frac{\{\{\rho\}\}}{2\{\{b\}\}}, \quad (\text{A.8})$$

$$c^* = \sqrt{\frac{p^*}{\{\{\rho\}\}_{\log}}}, \quad (\text{A.9})$$

$$h^* = \frac{\gamma}{2\{\{b\}\}_{\log}(\gamma - 1)} + \frac{\overline{u^2}}{2} + \{\{\phi\}\}, \quad (\text{A.10})$$

$$(\text{A.11})$$

and \mathbf{n} , \mathbf{m} , $\boldsymbol{\ell}$ are orthonormal vectors. The action of the dissipation operator on the jump in entropy variables can be written without having to specify non-uniquely defined tangent vectors \mathbf{m} and $\boldsymbol{\ell}$ as

$$(\mathbf{H}_n[\boldsymbol{\beta}])_\rho = w_1 + w_2 + w_3, \quad (\text{A.12})$$

$$\begin{aligned} (\mathbf{H}_n[\boldsymbol{\beta}])_{\rho u} &= (w_1(\{\{\mathbf{u}\}\} - c^*\mathbf{n}) + w_2\{\{\mathbf{u}\}\} + w_3(\{\{\mathbf{u}\}\} + c^*\mathbf{n}) \\ &\quad + |u_n|p^*\mathbf{T}([\boldsymbol{\beta}]_{\rho u} - \{\{\mathbf{u}\}\}[\boldsymbol{\beta}]_{\rho e})), \end{aligned} \quad (\text{A.13})$$

$$\begin{aligned} (\mathbf{H}_n[\boldsymbol{\beta}])_{\rho e} &= \left(w_1(h^* - c^*u_n) + w_2\left(\frac{\overline{u^2}}{2} + \{\{\phi\}\}\right) + w_3(h^* + c^*u_n) \right. \\ &\quad \left. + |u_n|p^*(\mathbf{T}\{\{\mathbf{u}\}\} \cdot [\boldsymbol{\beta}]_{\rho u} - \|\mathbf{T}\{\{\mathbf{u}\}\}\|_2^2[\boldsymbol{\beta}]_{\rho e}) \right), \end{aligned}$$

where

$$\mathbf{T} = \mathbf{I} - \mathbf{n} \otimes \mathbf{n}, \quad (\text{A.14})$$

$$w_1 = |u_n - c^*| \frac{\{\{\rho\}\}_{\log}}{2\gamma} \left([\boldsymbol{\beta}]_\rho + ([\mathbf{u}] - c^*\mathbf{n}) \cdot [\boldsymbol{\beta}]_{\rho u} + (h^* - c^*u_n)[\boldsymbol{\beta}]_{\rho e} \right), \quad (\text{A.15})$$

$$w_2 = |u_n| \frac{(\gamma - 1)\{\{\rho\}\}_{\log}}{\gamma} \left([\boldsymbol{\beta}]_\rho + \{\{\mathbf{u}\}\} \cdot [\boldsymbol{\beta}]_{\rho u} + \left(\frac{\overline{u^2}}{2} + \{\{\phi\}\}\right) [\boldsymbol{\beta}]_{\rho e} \right), \quad (\text{A.16})$$

$$w_3 = |u_n + c^*| \frac{\{\{\rho\}\}_{\log}}{2\gamma} \left([\boldsymbol{\beta}]_\rho + ([\mathbf{u}] + c^*\mathbf{n}) \cdot [\boldsymbol{\beta}]_{\rho u} + (h^* + c^*u_n)[\boldsymbol{\beta}]_{\rho e} \right), \quad (\text{A.17})$$

and $[\boldsymbol{\beta}]_\rho$, $[\boldsymbol{\beta}]_{\rho u}$, $[\boldsymbol{\beta}]_{\rho e}$ denotes $[\boldsymbol{\beta}]_1$, $([\boldsymbol{\beta}]_2, [\boldsymbol{\beta}]_3, [\boldsymbol{\beta}]_4)$, $[\boldsymbol{\beta}]_5$, respectively.

Appendix B. Well-balanced property for isothermal atmosphere

Here we prove that the new entropy-stable scheme is well-balanced for an isothermal atmosphere for an unwarped “box” domain. That is we assume that the domain is Ω is such that all the elements are aligned with ξ_3 being the direction that gravity acts and ξ_1 and ξ_2 are orthogonal. This is possible on, for instance, a perfect spherical shell domain with gravity acting radially or an unwarped hexahedral domain with gravity acting downward. In both cases we let r be the direction that gravity acts so that the geopotential is $\phi = gr$ where g is a constant. In each element we assume that $r \equiv r(\xi_3)$ so that ϕ is also only a function of ξ_3 . To demonstrate hydrostatic balance we show that the entropy conservative flux (76) is zero when the initial conditions are set to the analytic hydrostatic state for an isothermal atmosphere.

A hydrostatically balanced state is a state which is independent of time with a zero velocity and depends only on r . After assuming a stationary solution which only depends on r with $u_k = 0$, the atmospheric equations (1) reduce to the hydrostatic balance equation

$$\frac{\partial p}{\partial r} = -\rho g. \quad (\text{B.1})$$

Under the isothermal assumption of the ideal gas law $p = \rho R_d T_0$ with R_d and T_0 being the gas constant and constant reference temperature, respectively, we then have an exponential solution for pressure p and density ρ

$$p = p_0 \exp\left(-\frac{gr}{R_d T_0}\right), \quad (\text{B.2a})$$

$$\rho = \frac{p_0}{R_d T_0} \exp\left(-\frac{gr}{R_d T_0}\right), \quad (\text{B.2b})$$

where p_0 is the pressure at $r = 0$.

Since the solution only varies in r and thus is constant with respect to ξ_1 and ξ_2 in each element, consistency of a numerical flux in fluctuation form (41) implies that \mathcal{D}_1 and \mathcal{D}_2 are zero. The third component of the entropy conservative numerical flux (76) simplifies to

$$\mathcal{D}_3(\mathbf{q}^-, \mathbf{x}^-, \mathbf{q}^+, \mathbf{x}^+) = \begin{bmatrix} 0 \\ 0 \\ 0 \\ \left(p^* + \frac{1}{2}\hat{\rho}[[\phi]]\right) \\ 0 \end{bmatrix} - \begin{bmatrix} 0 \\ 0 \\ 0 \\ p^- \\ 0 \end{bmatrix}. \quad (\text{B.3})$$

Since in the balance solution (B.2) pressure is proportional to density the inverse temperature is constant, $b = \rho/2p = 1/R_d T_0$, and the expressions for the auxiliary variables (73b) and (73d) simplify to

$$p^* = \frac{R_d T_0}{2} \{\{\rho\}\}, \quad (\text{B.4a})$$

$$\hat{\rho} = \{\{\rho\}\}_{\log}. \quad (\text{B.4b})$$

Evaluating the density logarithmic average with the balanced density solution (B.2b) gives

$$\hat{\rho} = \frac{\rho^+ - \rho^-}{\log \rho^+ - \log \rho^-} = -R_d T_0 \frac{\rho^+ - \rho^-}{gr^+ - gr^-} = -R_d T_0 \frac{[[\rho]]}{[[\phi]]}. \quad (\text{B.5})$$

Using the auxiliary expressions (B.4a) and (B.5) in the non-zero term of the numerical flux (B.3) leads to

$$\left(p^* + \frac{1}{2}\hat{\rho}[[\phi]]\right) - p^- = \frac{R_d T_0}{2} \{\{\rho\}\} - \frac{R_d T_0}{2} [[\rho]] - p^- = R_d T_0 \rho^- - p^- = p^- - p^- = 0. \quad (\text{B.6})$$

This implies that \mathcal{D}_3 is zero and thus the solution is well-balanced.

References

- [1] Abdelfattah, A., Barra, V., Beams, N., Bleile, R., Brown, J., Camier, J.S., Carson, R., Chalmers, N., Dobrev, V., Dudouit, Y., et al.: GPU Algorithms for Efficient Exascale Discretizations. *Parallel Comput.* p. 102841 (2021). doi:[10.1016/j.parco.2021.102841](https://doi.org/10.1016/j.parco.2021.102841)
- [2] Abdi, D.S., Wilcox, L.C., Warburton, T.C., Giraldo, F.X.: A GPU-accelerated continuous and discontinuous Galerkin non-hydrostatic atmospheric model. *Int. J. High Perform. Comput. Appl.* **33**(1), 81–109 (2019). doi:[10.1177/1094342017694427](https://doi.org/10.1177/1094342017694427)
- [3] Baldauf, M.: A horizontally explicit, vertically implicit (HEVI) Discontinuous Galerkin scheme for the 2-dimensional Euler and Navier-Stokes equations using terrain-following coordinates. *J. Comput. Phys.* **446**, 110,635 (2021). doi:[10.1016/j.jcp.2021.110635](https://doi.org/10.1016/j.jcp.2021.110635)
- [4] Baldauf, M., Brdar, S.: An analytic solution for linear gravity waves in a channel as a test for numerical models using the non-hydrostatic, compressible Euler equations. *Q. J. Roy. Meteor. Soc.* **139**(677), 1977–1989 (2013). doi:[10.1002/qj.2105](https://doi.org/10.1002/qj.2105)
- [5] Beck, A.D., Bolemann, T., Flad, D., Frank, H., Gassner, G.J., Hindenlang, F., Munz, C.D.: High-order discontinuous Galerkin spectral element methods for transitional and turbulent flow simulations. *Int. J. Numer. Methods Fluids* **76**(8), 522–548 (2014). doi:[10.1002/fld.3943](https://doi.org/10.1002/fld.3943)
- [6] Biswas, B., Kumar, H., Yadav, A.: Entropy stable discontinuous Galerkin methods for ten-moment Gaussian closure equations. *J. Comput. Phys.* **431**, 110,148 (2021). doi:[10.1016/j.jcp.2021.110148](https://doi.org/10.1016/j.jcp.2021.110148)
- [7] Blaise, S., Lambrechts, J., Deleersnijder, E.: A stabilization for three-dimensional discontinuous Galerkin discretizations applied to nonhydrostatic atmospheric simulations. *Int. J. Numer. Methods Fluids* **81**(9), 558–585 (2016). doi:[10.1002/fld.4197](https://doi.org/10.1002/fld.4197)
- [8] Bohm, M., Winters, A.R., Gassner, G.J., Derigs, D., Hindenlang, F., Saur, J.: An entropy stable nodal discontinuous Galerkin method for the resistive MHD equations. Part I: Theory and numerical verification. *J. Comput. Phys.* **422**, 108,076 (2020). doi:[10.1016/j.jcp.2018.06.027](https://doi.org/10.1016/j.jcp.2018.06.027)
- [9] Carpenter, M.H., Fisher, T.C., Nielsen, E.J., Frankel, S.H.: Entropy Stable Spectral Collocation Schemes for the Navier–Stokes Equations: Discontinuous Interfaces. *SIAM J. Sci. Comput.* **36**(5), B835–B867 (2014). doi:[10.1137/130932193](https://doi.org/10.1137/130932193)
- [10] Carpenter, M.H., Kennedy, C.A.: Fourth-order 2N-storage Runge–Kutta schemes (1994)
- [11] Castro, M.J., Fjordholm, U.S., Mishra, S., Pares, C.: Entropy conservative and entropy stable schemes for nonconservative hyperbolic systems. *SIAM J. Numer. Anal.* **51**(3), 1371–1391 (2013). doi:[10.1137/110845379](https://doi.org/10.1137/110845379)
- [12] Castro, M.J., de Luna, T.M., Parés, C.: Well-balanced schemes and path-conservative numerical methods. In: *Handbook of Numerical Analysis*, vol. 18, pp. 131–175. Elsevier (2017). doi:[10.1016/bs.hna.2016.10.002](https://doi.org/10.1016/bs.hna.2016.10.002)
- [13] Chan, J.: On discretely entropy conservative and entropy stable discontinuous Galerkin methods. *J. Comput. Phys.* **362**, 346–374 (2018). doi:[10.1016/j.jcp.2018.02.033](https://doi.org/10.1016/j.jcp.2018.02.033)
- [14] Chan, J.: Skew-symmetric entropy stable modal discontinuous Galerkin formulations. *J. Sci. Comput.* **81**(1), 459–485 (2019). doi:[10.1007/s10915-019-01026-w](https://doi.org/10.1007/s10915-019-01026-w)
- [15] Chandrashekar, P.: Kinetic Energy Preserving and Entropy Stable Finite Volume Schemes for Compressible Euler and Navier-Stokes Equations. *Commun. Comput. Phys.* **14**(5), 1252–1286 (2013). doi:[10.4208/cicp.170712.010313a](https://doi.org/10.4208/cicp.170712.010313a)
- [16] Chen, T., Shu, C.W.: Entropy stable high order discontinuous Galerkin methods with suitable quadrature rules for hyperbolic conservation laws. *J. Comput. Phys.* **345**, 427–461 (2017). doi:[10.1016/j.jcp.2017.05.025](https://doi.org/10.1016/j.jcp.2017.05.025)
- [17] Chertock, A., Cui, S., Kurganov, A., Özcan, Ş.N., Tadmor, E.: Well-balanced schemes for the Euler equations with gravitation: Conservative formulation using global fluxes. *J. Comput. Phys.* **358**, 36–52 (2018). doi:[10.1016/j.jcp.2017.12.026](https://doi.org/10.1016/j.jcp.2017.12.026)
- [18] Coquel, F., Marmignon, C., Rai, P., Renac, F.: An entropy stable high-order discontinuous Galerkin spectral element method for the Baer-Nunziato two-phase flow model. *J. Comput. Phys.* **431**, 110,135 (2021). doi:[10.1016/j.jcp.2021.110135](https://doi.org/10.1016/j.jcp.2021.110135)
- [19] Dafermos, C.M.: *Hyperbolic Conservation Laws in Continuum Physics, Grundlehren der mathematischen Wissenschaften*, vol. 325. Third edition edn. Springer-Verlag, Berlin Heidelberg (2010). doi:[10.1007/978-3-642-04048-1](https://doi.org/10.1007/978-3-642-04048-1)
- [20] Derigs, D., Winters, A.R., Gassner, G.J., Walch, S.: A novel averaging technique for discrete entropy-stable dissipation operators for ideal MHD. *J. Comput. Phys.* **330**, 624–632 (2017). doi:[10.1016/j.jcp.2016.10.055](https://doi.org/10.1016/j.jcp.2016.10.055)
- [21] Duan, J., Tang, H.: High-order accurate entropy stable nodal discontinuous Galerkin schemes for the ideal special relativistic magnetohydrodynamics. *J. Comput. Phys.* **421**, 109,731 (2020). doi:[10.1016/j.jcp.2020.109731](https://doi.org/10.1016/j.jcp.2020.109731)
- [22] Fischer, P., Mullen, J.: Filter-based stabilization of spectral element methods. *Cr. Acad. Sci. I-Math* **332**(3), 265–270 (2001). doi:[10.1016/S0764-4442\(00\)01763-8](https://doi.org/10.1016/S0764-4442(00)01763-8)
- [23] Fisher, T.C., Carpenter, M.H.: High-order entropy stable finite difference schemes for nonlinear conservation laws: Finite domains. *J. Comput. Phys.* **252**, 518–557 (2013). doi:[10.1016/j.jcp.2013.06.014](https://doi.org/10.1016/j.jcp.2013.06.014)
- [24] Gassner, G.J.: A Skew-Symmetric Discontinuous Galerkin Spectral Element Discretization and Its Relation to SBP-SAT Finite Difference Methods. *SIAM J. Sci. Comput.* **35**(3), A1233–A1253 (2013). doi:[10.1137/120890144](https://doi.org/10.1137/120890144)
- [25] Gassner, G.J., Winters, A.R.: A novel robust strategy for discontinuous Galerkin methods in computational fluid mechanics: why? when? what? where? *Front. Phys.* **8**, 612 (2021). doi:[10.3389/fphy.2020.500690](https://doi.org/10.3389/fphy.2020.500690)
- [26] Gassner, G.J., Winters, A.R., Kopriva, D.A.: Split form nodal discontinuous Galerkin schemes with summation-by-parts property for the compressible Euler equations. *J. Comput. Phys.* **327**, 39–66 (2016). doi:[10.1016/j.jcp.2016.09.013](https://doi.org/10.1016/j.jcp.2016.09.013)
- [27] Giraldo, F.X.: *An Introduction to Element-based Galerkin Methods on Tensor-Product Bases - Analysis, Algorithms, and Applications*, vol. 24. Springer (2020)
- [28] Giraldo, F.X., Kelly, J.F., Constantinescu, E.M.: Implicit-explicit formulations of a three-dimensional nonhydrostatic unified model of the atmosphere (NUMA). *SIAM J. Sci. Comput.* **35**(5), B1162–B1194 (2013). doi:[10.1137/120876034](https://doi.org/10.1137/120876034)
- [29] Giraldo, F.X., Restelli, M.: A study of spectral element and discontinuous Galerkin methods for the Navier–Stokes equations in nonhydrostatic mesoscale atmospheric modeling: Equation sets and test cases. *J. Comput. Phys.* **227**(8), 3849–3877 (2008). doi:[10.1016/j.jcp.2007.12.009](https://doi.org/10.1016/j.jcp.2007.12.009)
- [30] Hesthaven, J.S., Warburton, T.: Nodal high-order methods on unstructured grids: I. Time-domain solution of Maxwell’s equations. *J. Comput. Phys.* **181**(1), 186–221 (2002). doi:[10.1006/jcph.2002.7118](https://doi.org/10.1006/jcph.2002.7118)
- [31] Ismail, F., Roe, P.L.: Affordable, entropy-consistent Euler flux functions II: Entropy production at shocks. *J. Comput. Phys.* **228**(15), 5410–5436 (2009). doi:[10.1016/j.jcp.2009.04.021](https://doi.org/10.1016/j.jcp.2009.04.021)
- [32] Kidder, L.E., Field, S.E., Foucart, F., Schnetter, E., Teukolsky, S.A., Bohn, A., Deppe, N., Diener, P., Hébert, F., Lippuner, J., et al.: SpECTRE: A task-based discontinuous Galerkin code for relativistic astrophysics. *J. Comput. Phys.* **335**, 84–114 (2017). doi:[10.1016/j.jcp.2016.12.059](https://doi.org/10.1016/j.jcp.2016.12.059)

- [33] Kolev, T., Fischer, P., Min, M., Dongarra, J., Brown, J., Dobrev, V., Warburton, T., Tomov, S., Shephard, M.S., Abdelfattah, A., et al.: Efficient exascale discretizations: High-order finite element methods. *Int. J. High Perform. Comput. Appl.* p. 10943420211020803 (2021). doi:[10.1177/10943420211020803](https://doi.org/10.1177/10943420211020803)
- [34] Kopriva, D.: *Implementing Spectral Methods for Partial Differential Equations*. Springer, New York (2009)
- [35] Kopriva, D.A.: Metric identities and the discontinuous spectral element method on curvilinear meshes. *J. Sci. Comput.* **26**(3), 301–327 (2006). doi:[10.1007/s10915-005-9070-8](https://doi.org/10.1007/s10915-005-9070-8)
- [36] Kopriva, D.A., Gassner, G.J.: An energy stable discontinuous Galerkin spectral element discretization for variable coefficient advection problems. *SIAM J. Sci. Comput.* **36**(4), A2076–A2099 (2014). doi:[10.1137/130928650](https://doi.org/10.1137/130928650)
- [37] Krivodonova, L.: Limiters for high-order discontinuous Galerkin methods. *J. Comput. Phys.* **226**(1), 879–896 (2007). doi:[10.1016/j.jcp.2007.05.011](https://doi.org/10.1016/j.jcp.2007.05.011)
- [38] Liu, Y., Shu, C.W., Zhang, M.: Entropy stable high order discontinuous Galerkin methods for ideal compressible MHD on structured meshes. *J. Comput. Phys.* **354**, 163–178 (2018). doi:[10.1016/j.jcp.2017.10.043](https://doi.org/10.1016/j.jcp.2017.10.043)
- [39] Luo, J., Xu, K., Liu, N.: A well-balanced symplecticity-preserving gas-kinetic scheme for hydrodynamic equations under gravitational field. *SIAM J. Sci. Comput.* **33**(5), 2356–2381 (2011). doi:[10.1137/100803699](https://doi.org/10.1137/100803699)
- [40] Marras, S., Kelly, J.F., Moragues, M., Müller, A., Koper, M.A., Vázquez, M., Giraldo, F.X., Houzeaux, G., Jorba, O.: A review of element-based Galerkin methods for numerical weather prediction: Finite elements, spectral elements, and discontinuous Galerkin. *Arch. Comput. Methods E.* **23**(4), 673–722 (2016). doi:[10.1007/s11831-015-9152-1](https://doi.org/10.1007/s11831-015-9152-1)
- [41] Mengaldo, G., De Grazia, D., Moxey, D., Vincent, P.E., Sherwin, S.J.: Dealiasing techniques for high-order spectral element methods on regular and irregular grids. *J. Comput. Phys.* **299**, 56–81 (2015). doi:[10.1016/j.jcp.2015.06.032](https://doi.org/10.1016/j.jcp.2015.06.032)
- [42] Müller, A., Koper, M.A., Marras, S., Wilcox, L.C., Isaac, T., Giraldo, F.X.: Strong scaling for numerical weather prediction at petascale with the atmospheric model NUMA. *Int. J. High Perform. Comput. Appl.* **33**(2), 411–426 (2019). doi:[10.1177/1094342018763966](https://doi.org/10.1177/1094342018763966)
- [43] Qiu, J., Shu, C.W.: Runge–Kutta discontinuous Galerkin method using WENO limiters. *SIAM J. Sci. Comput.* **26**(3), 907–929 (2005). doi:[10.1137/S1064827503425298](https://doi.org/10.1137/S1064827503425298)
- [44] Ranocha, H.: Comparison of some entropy conservative numerical fluxes for the Euler equations. *J. Sci. Comput.* **76**(1), 216–242 (2018). doi:[10.1007/s10915-017-0618-1](https://doi.org/10.1007/s10915-017-0618-1)
- [45] Ranocha, H.: Generalised summation-by-parts operators and variable coefficients. *J. Comput. Phys.* **362**, 20–48 (2018). doi:[10.1016/j.jcp.2018.02.021](https://doi.org/10.1016/j.jcp.2018.02.021)
- [46] Ranocha, H., Sayyari, M., Dalcin, L., Parsani, M., Ketcheson, D.I.: Relaxation Runge–Kutta Methods: Fully Discrete Explicit Entropy-Stable Schemes for the Compressible Euler and Navier–Stokes Equations. *SIAM J. Sci. Comput.* **42**(2), A612–A638 (2020). doi:[10.1137/19M1263480](https://doi.org/10.1137/19M1263480)
- [47] Renac, F.: Entropy stable DGSEM for nonlinear hyperbolic systems in nonconservative form with application to two-phase flows. *J. Comput. Phys.* **382**, 1–26 (2019). doi:[10.1016/j.jcp.2018.12.035](https://doi.org/10.1016/j.jcp.2018.12.035)
- [48] Renac, F.: Entropy stable, robust and high-order DGSEM for the compressible multicomponent Euler equations. *J. Comput. Phys.* **445**, 110,584 (2021). doi:[10.1016/j.jcp.2021.110584](https://doi.org/10.1016/j.jcp.2021.110584)
- [49] Rojas, D., Boukharfane, R., Dalcin, L., Fernández, D.C.D.R., Ranocha, H., Keyes, D.E., Parsani, M.: On the robustness and performance of entropy stable collocated discontinuous Galerkin methods. *J. Comput. Phys.* **426**, 109,891 (2021). doi:[10.1016/j.jcp.2020.109891](https://doi.org/10.1016/j.jcp.2020.109891)
- [50] Schaal, K., Bauer, A., Chandrashekar, P., Pakmor, R., Klingenberg, C., Springel, V.: Astrophysical hydrodynamics with a high-order discontinuous Galerkin scheme and adaptive mesh refinement. *Mon. Not. R. Astron. Soc.* **453**(4), 4278–4300 (2015). doi:[10.1093/mnras/stv1859](https://doi.org/10.1093/mnras/stv1859)
- [51] Skamarock, W.C., Ong, H., Klemp, J.B.: A Fully Compressible Nonhydrostatic Deep-Atmosphere Equations Solver for MPAS. *Mon. Weather Rev.* **149**(2), 571–583 (2021). doi:[10.1175/MWR-D-20-0286.1](https://doi.org/10.1175/MWR-D-20-0286.1)
- [52] Smolarkiewicz, P.K., Pudykiewicz, J.A.: A class of semi-Lagrangian approximations for fluids. *J. Atmos. Sci.* **49**(22), 2082–2096 (1992). doi:[10.1175/1520-0469\(1992\)049<2082:ACOSLA>2.0.CO;2](https://doi.org/10.1175/1520-0469(1992)049<2082:ACOSLA>2.0.CO;2)
- [53] Smolarkiewicz, P.K., Szmelter, J.: Iterated upwind schemes for gas dynamics. *J. Comput. Phys.* **228**(1), 33–54 (2009). doi:[10.1016/j.jcp.2008.08.008](https://doi.org/10.1016/j.jcp.2008.08.008)
- [54] Svärd, M.: Entropy stable boundary conditions for the Euler equations. *J. Comput. Phys.* **426**, 109,947 (2021). doi:[10.1016/j.jcp.2020.109947](https://doi.org/10.1016/j.jcp.2020.109947)
- [55] Tadmor, E.: The numerical viscosity of entropy stable schemes for systems of conservation laws. I. *Math. Comput.* **49**(179), 91–103 (1987). doi:[10.2307/2008251](https://doi.org/10.2307/2008251)
- [56] Taylor, M.A., Guba, O., Steyer, A., Ullrich, P.A., Hall, D.M., Eldrid, C.: An energy consistent discretization of the nonhydrostatic equations in primitive variables. *J. Adv. Model. Earth Sy.* **12**(1) (2020). doi:[10.1029/2019MS001783](https://doi.org/10.1029/2019MS001783)
- [57] Thomas, P., Lombard, C.: Geometric conservation law and its application to flow computations on moving grids. *AIAA J.* **17**(10), 1030–1037 (1979). doi:[10.2514/3.61273](https://doi.org/10.2514/3.61273)
- [58] Tumolo, G., Bonaventura, L.: A semi-implicit, semi-Lagrangian discontinuous Galerkin framework for adaptive numerical weather prediction. *Q. J. Roy. Meteor. Soc.* **141**(692), 2582–2601 (2015). doi:[10.1002/qj.2544](https://doi.org/10.1002/qj.2544)
- [59] Ullrich, P.A., Jablonowski, C., Reed, K.A., Zarzycki, C., Lauritzen, P.H., Nair, R.D., Kent, J., Verlet-Banide, A.: Dynamical core model intercomparison project (DCMIP2016) test case document (2016). URL <https://github.com/ClimateGlobalChange/DCMIP2016>
- [60] Ullrich, P.A., Melvin, T., Jablonowski, C., Staniforth, A.: A proposed baroclinic wave test case for deep- and shallow-atmosphere dynamical cores. *Q. J. Roy. Meteor. Soc.* **140**(682), 1590–1602 (2013). doi:[10.1002/qj.2241](https://doi.org/10.1002/qj.2241)
- [61] Ullrich, P.A., Reynolds, D.R., Guerra, J.E., Taylor, M.A.: Impact and importance of hyperdiffusion on the spectral element method: A linear dispersion analysis. *J. Comput. Phys.* **375**, 427–446 (2018). doi:[10.1016/j.jcp.2018.06.035](https://doi.org/10.1016/j.jcp.2018.06.035)
- [62] Warburton, T.: A low storage curvilinear discontinuous Galerkin time-domain method for electromagnetics. In: 2010 URSI International Symposium on Electromagnetic Theory, pp. 996–999 (2010). doi:[10.1109/URSI-EMTS.2010.5637392](https://doi.org/10.1109/URSI-EMTS.2010.5637392)
- [63] Wintermeyer, N., Winters, A.R., Gassner, G.J., Kopriva, D.A.: An entropy stable nodal discontinuous Galerkin method for the two dimensional shallow water equations on unstructured curvilinear meshes with discontinuous bathymetry. *J. Comput. Phys.* **340**, 200–242 (2017). doi:[10.1016/j.jcp.2017.03.036](https://doi.org/10.1016/j.jcp.2017.03.036)
- [64] Winters, A.R., Derigs, D., Gassner, G.J., Walch, S.: A uniquely defined entropy stable matrix dissipation operator for high Mach number ideal MHD and compressible Euler simulations. *J. Comput. Phys.* **332**, 274–289 (2017). doi:[10.1016/j.jcp.2016.12.006](https://doi.org/10.1016/j.jcp.2016.12.006)

- [65] Yu, J., Hesthaven, J.S.: A study of several artificial viscosity models within the discontinuous Galerkin framework. *Commun. Comput. Phys.* **27**(5), 1309–1343 (2020). doi:[10.4208/cicp.OA-2019-0118](https://doi.org/10.4208/cicp.OA-2019-0118)